Strong diffraction effects accompany the transmission of a laser beam through inhomogeneous plasma microstructures

E. V. Parkevich,[1,*] A. I. Khirianova,[1] T. F. Khirianov,[1] K. T. Smaznova,[1] D. V. Tolbukhin,[1,2] V. M. Romanova,[1] I. A. Kozin,[1] and S. A. Ambrozevich[3]

[1]*P. N. Lebedev Physical Institute of the Russian Academy of Sciences, 53 Leninskiy Prospekt, Moscow 119991, Russia*

[2]*Moscow Institute of Physics and Technology, Institutskiy Pereulok 9, Dolgoprudny, Moscow Region 141700, Russia*

[3]*Bauman Moscow State Technical University, 5/1 2-ya Baumanskaya St., Moscow 105005, Russia*

(Received 16 April 2023; revised 17 January 2024; accepted 1 April 2024; published 14 May 2024)

In the study we thoroughly analyze diffraction effects accompanying the laser beam transmission through inhomogeneous plasma microstructures and simulate their diffraction patterns at the object output and in the near field. For this we solve the scalar Helmholtz wave equation in the first Rytov approximation and compute the diffraction spreading of the transmitted beam in free space. Diffraction effects are found to arise within the beam passage through inhomogeneous plasma microstructures even in the simplest approximations of the laser beam interaction with plasma. These effects become strong in the near-field region and significantly distort the patterns of plasma formations, as well as facilitate the appearance of various optical artifacts in the plasma images. By performing numerical simulations, we characterize in detail the features of the visualization of plasma formations in the field of a coherent laser beam registered by a lens system. The calculations are in good agreement with the experimental data. The study can find broad applications in the processing of the laser images of plasma microstructures registered by lens systems in the presence of strong diffraction effects.

DOI: 10.1103/PhysRevE.109.055204

I. INTRODUCTION

Rapidly evolving plasma microstructures are the most challenging entities for optical measurements. This is stipulated by the short temporal and spatial scales of the plasma evolution, the bright glow of plasma in a wide spectral range, the technical difficulties in setting up experiments in terms of precise launching diagnosing equipment, etc. An efficient method to investigate plasma properties can be implemented through the plasma interaction with a coherent laser beam. By registering the changes in the beam characteristics (intensity, phase, polarization) behind the investigated plasma formation, one can construct the asymptotic solutions of inverse diffraction (scattering) problems and restore the distribution of a plasma refractive index [1–4]. The changes in the characteristics of a probing laser beam can be evaluated by classical interferometry, shadow and Schlieren photography, which have long become powerful tools of many optical studies [5–13]. Certain difficulties arise when constructing consistent models of a dielectric permittivity of the considered plasma. Here one should estimate the possible absorption [14–17], resonance [18], and other nonlinear [19] effects caused by the laser interaction with plasma. In some cases, during the passage through plasma with high gradients of the refractive index, the polarization of a probing laser beam can be disturbed [20,21]. Apart from this, plasma can be multicomponent and consist of multiple tiny particles (cases in point are the products of metal conductors exploded in vacuum, gases, and liquids [22]) enhancing the Rayleigh scattering [23,24] of the transmitted laser beam. If the influence of the mentioned effects is weak, then the plasma dielectric permittivity is real and determined by the plasma and radiation frequencies only. In other words, plasma can be considered as a purely phase object.

However, even in such a seemingly simple case strong diffraction effects can accompany the laser beam transmission through an inhomogeneous plasma. For instance, due to such effects, a very high contrast of the electric spark microstructure is reached in laser shadowgrams [25–29]. Strong diffraction effects can be also observed when laser radiation passes through a sharp boundary between plasma and its surrounding shock wave. This situation is inherent to plasma jets in plasma focus [30,31], laser and high-current electric sparks [32–35]. The diffraction effects can appear when imaging plasma ejections resulted from the interaction of a high-power laser pulse with a certain target [36–40], or cathode and anode spots at electrodes in an electric gas discharge [25,41]. In the approximation of a purely phase object the intensity of the diffracted laser beam is assumed to vary slightly in the output plane of the object and near it. At the same time experimental observations indicate that the radiation characteristics can undergo significant changes at a certain distance behind the object in its near-field region. In particular, when imaging plasma microstructures by an optical registration system, local zones with significant enhancements ("bright regions") and attenuations ("dark regions") of the radiation intensity can be recorded in laser shadowgrams. The appearance of such zones, actually driven by strong diffraction of a probing laser beam, in the near-field region is not obvious in terms of the

*parkevich@phystech.edu

classical approaches [42,43] used to analyze the laser beam transmission through plasma.

Unfortunately, laser beam diffraction by inhomogeneous plasma microstructures in their near-field region receives a little attention in modern experimental studies, which involve laser probing diagnostics. Although, in the near field the in-depth analysis of the laser beam characteristics is crucial for the processing of the plasma images [44]. Here the key problem is that the comprehensive theory currently does not exist to describe the observed characteristics of laser radiation diffracted by plasma microstructures. As a result, many interesting features of laser beam diffraction by plasma are dismissed and not interpreted in experiments, while being associated with irrelevant optical artifacts. Thus, the near-field analysis of laser diffraction by various plasma microstructures is of high relevance together with numerical simulations.

In this paper we evaluate diffraction of a plane optical wave by inhomogeneous plasma filaments with smooth boundaries having different diameters, shapes of the electron density distribution, and maximum values of the electron density. The simulations are performed for the 532 nm and 1064 nm wavelengths and supplemented with modeling of the image formation process in a lens system. Important wave effects accompanying laser diffraction by inhomogeneous plasma microstructures in their near-field region are established and verified in experiments. The contribution of the arising diffraction effects to the high-contrast visualization of the plasma formations is quantitatively estimated. The findings reveal their high efficiency in the analysis of the laser images of real plasma formations registered by lens systems.

II. THEORY OF WAVE DIFFRACTION BY PLASMA

A. Problem statement

In many optical measurements involving probing laser radiation the latter can be considered in the plane wave approximation if a small-sized plasma object is exposed to a low-divergence beam, with its diameter being much wider than the characteristic transverse dimensions of the object. We also assume an illuminated plasma object to be described by a continuous function of dielectric permittivity $\varepsilon(x, y, z)$ with smooth boundaries (dielectric permittivity does not change during the laser probing). In the study we restrict ourselves to the objects having axial symmetry, although the equations given below allow one to consider the direct diffraction problem for arbitrary objects. The medium surrounding the plasma is considered to be homogeneous and isotropic, and its average dielectric permittivity is taken to be constant $\langle\varepsilon\rangle = 1$. We exclude any absorption, resonance, and other nonlinear effects during the passage of a plane wave through the plasma. The latter is also considered to be unmagnetized, and its electron density is assumed to be far from the critical one (no wave reflection and back scattering). We also omit the hydrodynamic expansion of the plasma particles to the object boundary during the laser probing (which is relevant for short beams) and assume that the contribution of the neutral component of the plasma to the resultant dielectric permittivity is negligible (compared to that provided by the electron component). With the assumptions made the plasma dielectric

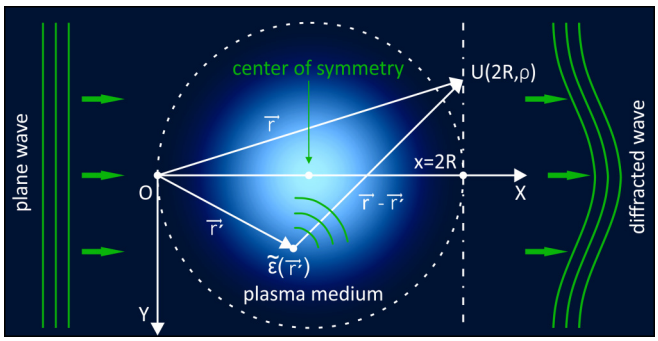

FIG. 1. Diffraction of a plane wave by a plasma formation.

permittivity can be expressed as [45]

$$\varepsilon = 1 - \omega_{pe}^2/\omega^2, \tag{1}$$

where $\omega_{pe} = (4\pi e^2 n_e/m_e)^{1/2}$ and ω are the plasma and radiation frequencies.

Let us introduce the Cartesian coordinate system xyz so that its center O coincides with the input plane (with the coordinate of $x = 0$) of the object, see Fig. 1, and direct along the Ox axis plane monochromatic wave $\sqrt{I_0}\exp(-i\omega t + ikx)$ (we use this form of writing a complex wave [46]) with intensity I_0, wave number $k = 2\pi/\lambda$, wavelength λ, and frequency ω. Thereinafter, multiplier $\exp(-i\omega t)$ is omitted. The changes in the intensity and phase of the wave will be analyzed in the yz plane, and we will also assume that the characteristics of the diffracted wave undergo final changes in the object output plane (with the coordinate of $x = 2R$). For the model plasma objects, which are considered in this study, parameter R serves as the object radius.

B. First Rytov approximation

Wave diffraction by a plasma formation can be described by solving the scalar Helmholtz wave equation [47]

$$\triangle\, U(x, \rho) + k^2(1 + \widetilde{\varepsilon}(x, \rho))U(x, \rho) = 0. \tag{2}$$

Here $U(x, \rho)$ is the scalar complex amplitude of the wave electric field vector, and dielectric permittivity is presented as $\varepsilon(x, \rho) = 1 + \widetilde{\varepsilon}(x, \rho)$, where $\widetilde{\varepsilon} = -\omega_{pe}^2/\omega^2$. For variables y and z two-dimensional variable $\rho = \sqrt{y^2 + z^2}$ is introduced. In the study we will additionally assume that the value of $\widetilde{\varepsilon}$ is rather small compared to unity, which is a characteristic of many plasma objects encountered in experiments. The object region is considered in terms of local fluctuations of the environment.

The employment of wave equation (2) is relevant when $\partial\widetilde{\varepsilon}/\partial t$ changes negligibly during the object probing, and typical scale $l_{\widetilde{\varepsilon}}$ (its value is of the order of $\widetilde{\varepsilon}/|\vec{\nabla}\widetilde{\varepsilon}|$) of the changes in function $\widetilde{\varepsilon}$ is greater than λ, i.e., $\lambda \ll l_{\widetilde{\varepsilon}}$. In other words, the transverse size of the object should be much greater than the radiation wavelength. For micrometer-sized plasma formations with smooth boundaries inequality $\lambda \ll l_{\widetilde{\varepsilon}}$ is fulfilled.

According to the original Rytov's approach to describe the solution of wave equation (2), complex amplitude $U(x, \rho)$ of

the wave is replaced by a function of complex phase $\Phi(x,\rho)$, which is defined as follows:

$$U(x,\rho)=\sqrt{I_0}e^{\Phi(x,\rho)}, \tag{3}$$

$$\Phi(x,\rho)=ikx+i\delta\phi(x,\rho)+\ln(\sqrt{I(x,\rho)/I_0}). \tag{4}$$

Function $\delta\phi(x,\rho)$ describes the acquired phase shift, and function $\ln(\sqrt{I(x,\rho)/I_0})$ is understood as the wave level, in which $I(x,\rho)$ and I_0 are the intensities of the diffracted wave and wave incident on the object. Proceeding to the function of the complex phase, Eq. (2) takes the form

$$\Delta\Phi+(\vec{\nabla}\Phi)^2+k^2+k^2\widetilde{\varepsilon}=0, \tag{5}$$

wherein $\widetilde{\varepsilon}$ is included additively, and the differentiation operators are $\triangle=\partial^2/\partial x^2+\partial^2/\partial y^2+\partial^2/\partial z^2$ and $\vec{\nabla}=\vec{h}^x\partial/\partial x+\vec{h}^y\partial/\partial y+\vec{h}^z\partial/\partial z$.

Equation (5) is solved in terms of the smooth perturbation method, which relies on the construction of an asymptotic series for the complex phase

$$\Phi=\Phi^{(0)}+\sigma_{\widetilde{\varepsilon}}\Phi^{(1)}+\sigma_{\widetilde{\varepsilon}}^2\Phi^{(2)}+\dots, \tag{6}$$

with decreasing order of terms with $m\geqslant 1$ containing small parameter $\sigma_{\widetilde{\varepsilon}}^m=\langle\widetilde{\varepsilon}^2\rangle^{m/2}$. Here $\sigma_{\widetilde{\varepsilon}}=\sqrt{\langle\widetilde{\varepsilon}^2\rangle}=\sqrt{\langle[\widetilde{\varepsilon}-\langle\widetilde{\varepsilon}\rangle]^2\rangle}$ appears as the standard deviation of $\widetilde{\varepsilon}$, with $\langle\widetilde{\varepsilon}\rangle=1/V\int_V\widetilde{\varepsilon}dV$ being the average value of $\widetilde{\varepsilon}$ computed for volume V with the useful information. Symbol $\langle\dots\rangle$ denotes averaging over the volume. In Eq. (6) zero term $\Phi^{(0)}$ describes wave propagation in the unperturbed medium, first $\Phi^{(1)}$ and second $\Phi^{(2)}$ terms appear as the solutions of wave equation (5) in the first and second Rytov approximations, respectively.

By substituting Eq. (6) in Eq. (5) and combining the terms with similar $\sigma_{\widetilde{\varepsilon}}^m$, one can obtain the infinite equation system

$$\Delta\Phi^{(0)}+(\vec{\nabla}\Phi^{(0)})^2=-k^2, \tag{7}$$

$$\Delta\Phi^{(1)}+2\vec{\nabla}\Phi^{(0)}\cdot\vec{\nabla}\Phi^{(1)}=-k^2\widetilde{\varepsilon}/\sigma_{\widetilde{\varepsilon}}, \tag{8}$$

$$\Delta\Phi^{(2)}+2\vec{\nabla}\Phi^{(0)}\cdot\vec{\nabla}\Phi^{(2)}=-k^2(\vec{\nabla}\Phi^{(1)})^2/\sigma_{\widetilde{\varepsilon}}^2, \tag{9}$$

....

The solution of each equation of the system can be expressed as [47]

$$\Phi^{(m)}(x,\rho)=-\frac{1}{4\pi}\iiint_{-\infty}^{+\infty}\frac{1}{|\vec{r}-\vec{r}'|}\exp(ik|\vec{r}-\vec{r}'|)\times\exp(ik(x'-x))F_m(x',\vec{r}')d^3r'. \tag{10}$$

Here F_m stands for the term in the right side of the considered equation of the system. The solution for Eq. (5) is obtained as $\Phi=\Phi_0+\Phi_1+\Phi_2+\dots$, where $\Phi_0=\Phi^{(0)}$, $\Phi_1=\sigma_{\widetilde{\varepsilon}}\Phi^{(1)}$, $\Phi_2=\sigma_{\widetilde{\varepsilon}}^2\Phi^{(2)}$, etc.

To evaluate wave diffraction by the plasma it is convenient to simplify integral (10). The simplification is based on taking into account the smallness of wave diffraction angle $\theta\approx\lambda/l_{\widetilde{\varepsilon}}$ because of the initially made assumption that $\lambda\ll l_{\widetilde{\varepsilon}}$ and the fact that in the approximations made wave back diffraction is negligible. These features allow for integration in Eq. (10) not from minus infinity but in the layer $[0,x]$ with boundary condition $\Phi^{(m)}(0,\rho)=0$ for each $m\geqslant 1$. In turn the exponent power in the Green's function can be approximated with the second term of the Taylor series for $k|\vec{r}-\vec{r}'|\approx k[(x-x')+(\rho-\rho')^2/2(x-x')]$

$$\Phi^{(m)}(x,\rho)=-\frac{1}{4\pi}\int_0^x\frac{1}{x-x'}dx'\times\iint_{-\infty}^{+\infty}\exp\left(\frac{ik(\rho-\rho')^2}{2(x-x')}\right)F_m(x',\rho')d^2\rho', \tag{11}$$

if $k(\rho-\rho')^4/8(x-x')^3\ll 1$ or, what is the same thing, provided that

$$\lambda(x-x')/l_{\widetilde{\varepsilon}}^2\ll(l_{\widetilde{\varepsilon}}/\lambda)^2. \tag{12}$$

Here we used the fact that the diffracted wave propagates at small angle θ with respect to the Ox axis, and $(\rho-\rho')/(x-x')\sim\theta\sim\lambda/l_{\widetilde{\varepsilon}}\ll 1$. In Eq. (11) the denominator in the Green's function is taken equal to first term $(x-x')$ of the Taylor series, with the corresponding relative error being of the order of $\lambda/l_{\widetilde{\varepsilon}}$. Integral (11) appears as the solution of Eq. (5) under the parabolic approximation [48]

$$2ik\frac{\partial\Phi}{\partial x}+\Delta_\perp\Phi+(\vec{\nabla}_\perp\Phi)^2+k^2\widetilde{\varepsilon}=0. \tag{13}$$

Here differentiation operators $\Delta_\perp=\partial^2/\partial y^2+\partial^2/\partial z^2$ and $\vec{\nabla}_\perp=\vec{h}^y\partial/\partial y+\vec{h}^z\partial/\partial z$ are used to simplify the form of the parabolic equation.

Notably, the smooth perturbation method requires the decrease in the magnitudes of each successive term in Eq. (6), which makes the series to converge. In the original Rytov's theory [48], on the one hand, it is proposed to construct the series of the complex phase by expanding it in the powers of standard deviation $\sigma_{\widetilde{\varepsilon}}$ of the dielectric permittivity, which appears as a small parameter. On the other hand, Φ_1 is selected in such a manner as to differ little from Φ and be the same order of smallness with respect to $\widetilde{\varepsilon}$. Such an approach is similar to the first Born approximation [1,49,50]. Therefore, in the parabolic approximation the following restriction on Φ_1 is imposed (see Ref. [48])

$$\langle|\vec{\nabla}_\perp\Phi_1|^2\rangle=1/V\int_V|\vec{\nabla}_\perp\Phi_1|^2dV\ll k^2\sigma_{\widetilde{\varepsilon}}. \tag{14}$$

Since Φ_1 is the complex function, in Eq. (14) the absolute value of $|\vec{\nabla}_\perp\Phi_1|$ is taken. The restriction means that at transverse distances of the order of λ first term Φ_1 of the complex phase series changes much less than $\sigma_{\widetilde{\varepsilon}}$, i.e., a sufficient smoothness of the changes in functions Φ_1 and $\widetilde{\varepsilon}$ is required. Restriction (14) provides a gradual decrease in the magnitudes of the series' terms in view of the iterative determination of each term through the previous one. At the same time, we note that the convergence condition of the series based on restriction (14) is quite strict and in some cases can be significantly simplified. Looking ahead and not discussing the problem of the series convergence in detail, we note that condition (14) is well fulfilled for the plasma objects considered in this study.

Equation (13) can be easily reduced to the iterative equation system, which is more practical for numerical simulations. To this end, let us introduce two-dimensional Fourier transforms $\Psi_1=\mathcal{F}(\Phi_1)$, $\Psi_2=\mathcal{F}(\Phi_2)$, ..., $\Lambda=\mathcal{F}(\widetilde{\varepsilon})$, $X=\mathcal{F}((\vec{\nabla}\Phi_1)^2)$, ...of functions Φ_1, Φ_2, ..., and $\widetilde{\varepsilon}$, $(\vec{\nabla}\Phi_1)^2$, ..., etc.

Such an approach has a number of advantages, in particular the Fourier transforms (direct $\mathcal{F}$ and inverse $\mathcal{F}^{-1}$) are easy realized in the already elaborated libraries integrated with different programming languages. By substituting transforms Ψ_m in Eq. (13), one can obtain the following equation system:

$$2ik\frac{\partial \Psi_1}{\partial x} - (2\pi f_\rho)^2 \Psi_1 = -k^2 \Lambda, \tag{15}$$

$$2ik\frac{\partial \Psi_2}{\partial x} - (2\pi f_\rho)^2 \Psi_2 = -X, \tag{16}$$

$$\ldots\ldots\ldots\ldots\ldots\ldots\ldots\ldots,$$

where terms Ψ_m and functions Λ, X, ... are defined as

$$\Psi_m(x,\rho) = \iint_{-\infty}^{+\infty} \Phi_m(x,\rho) e^{-2\pi i \rho f_\rho} d\rho, \tag{17}$$

$$\Lambda(x,\rho) = \iint_{-\infty}^{+\infty} \widetilde{\varepsilon}(x,\rho) e^{-2\pi i \rho f_\rho} d\rho, \tag{18}$$

$$X(x,\rho) = \iint_{-\infty}^{+\infty} \left(\vec{\nabla}_\perp \Phi_1(x,\rho)\right)^2 e^{-2\pi i \rho f_\rho} d\rho, \tag{19}$$

$$\ldots\ldots\ldots\ldots\ldots\ldots\ldots\ldots.$$

As a result the obtained equations with terms Ψ_m can be solved in the form being more favorable for numerical simulations [47,48]

$$\Psi_1(x, f_\rho) = -\frac{k}{2i}\int_0^x \Lambda(x', f_\rho) e^{-i\lambda\pi(x-x')f_\rho^2} dx', \tag{20}$$

$$\Psi_2(x, f_\rho) = -\frac{1}{2ik}\int_0^x X(x', f_\rho) e^{-i\lambda\pi(x-x')f_\rho^2} dx', \tag{21}$$

$$\ldots\ldots\ldots\ldots\ldots\ldots\ldots\ldots.$$

Here $f_\rho = (f_y^2 + f_z^2)^{1/2}$, and variables f_y and f_z are the spatial frequencies related to the coordinates y and z.

The phase shift $\delta\phi = \delta\phi_1 + \delta\phi_2 + \ldots$ and intensity $I = I_1 \times I_2 \times \ldots$ of the diffracted wave, as well as their corrections determined by the high-order terms of the infinite series, are obtained from equations

$$\delta\phi_m(x, f_\rho) = \mathtt{Im}(\mathcal{F}^{-1}(\Psi_m)), \tag{22}$$

$$I_m(x, f_\rho) = I_0 \times \mathtt{exp}[2 \times \mathtt{Re}(\mathcal{F}^{-1}(\Psi_m))]. \tag{23}$$

Hereinafter the value of I_0 equals to unity.

Thus, by computing Eqs. (20)–(23), one can simulate wave diffraction by a plasma formation, with the diffraction spreading of the wave front automatically taken into account during the wave transmission through the plasma. Note that these equations allow one to calculate wave diffraction behind the plasma object in free space. However, this turns out to be a computationally intensive procedure with the employment of a small grid spacing. It is more convenient to take advantage of a spectral convolution described in the section below.

C. Diffraction in free space

Wave diffraction behind a plasma object can be described by simulating convolution

$$U(x+\Delta x, \rho) = \mathcal{F}^{-1}(\mathcal{F}(U(x,\rho)) \times P(\Delta x, f_\rho)). \tag{24}$$

Here function $U(x,\rho) = \sqrt{I(x,\rho)}\exp(i\delta\phi(x,\rho))$ is the complex amplitude of the wave calculated in the output plane (with the coordinate of $x = 2R$) of the object. The essence of the convolution is as follows. First, a two-dimensional Fourier transform (direct $\mathcal{F}$) is applied to complex wave $U(x,\rho)$. The image $\mathcal{F}(U(x,\rho))$ is multiplied by operator $P(\Delta x, f_\rho) = \exp[2\pi i \Delta x(\lambda^{-2} - f_\rho^2)^{1/2}]$ describing the propagation of the wave angular spectrum in free space [51]. The variable Δx is the distance between the initial plane and that of interest. The result of the multiplication is further translated into a coordinate representation by applying the inverse ($\mathcal{F}^{-1}$) Fourier transform. Finally, in the plane of interest wave field $U(x+\Delta x,\rho)$ and its phase shift $\delta\phi(x+\Delta x,\rho)$ and intensity $I(x+\Delta x,\rho)$ are obtained.

III. NUMERICAL RESULTS

Many interesting plasma formations observed in experiments can be associated with model objects having cylindrical or spherical symmetry. Apart from symmetry, other important characteristics of the object are the shape of the plasma dielectric permittivity and the degree of smoothness of the object boundary. In the current study we restrict ourselves to filaments of highly ionized plasma with micrometer-sized diameters and smooth boundaries and consider diffraction of a plane wave in the visible ($\lambda = 532$ nm) and infrared ($\lambda = 1064$ nm) wavelength ranges, which are important from a practical point of view.

A. Diffracted wave in the output plane of a plasma filament

Let us consider a model profile of the electron density, see Fig. 2(a). The profile is $n_e(y) = A(1+\cos(\pi y/R))/2$, has axial symmetry in $x = R$, and is associated with a plasma filament with a diameter of $2R = 20\,\mu$m. Here $A = 5 \times 10^{19}$ cm^{-3} is the dimension factor. The profile $n_e(y)$ is chosen as close as possible to the experimental distributions of thin plasma filaments obtained in Ref. [26], see also the comments in Appendix A. In Fig. 2(a) there are also the distributions of refractive index $n_{\mathrm{ref}} = \sqrt{\varepsilon}$ and permittivity ε of the plasma filament calculated for wavelengths $\lambda = 532$ nm and $\lambda = 1064$ nm. Figure 2(b) demonstrates phase shift $\delta\phi_1(y)$ and intensity $I_1(y)$ of the diffracted plane wave in the filament output plane ($x = 2R$). The distributions are obtained by computing equation (20) with a grid step of 0.1 μm and 1 μm in the transverse and longitudinal directions. In spite of insignificant changes (no higher than ≈2% and ≈3.7%) in the minimum values of n_{ref} and ε, as the wavelength increases, the absolute value of maximum phase shift $\delta\phi_1^{\max}$ (≈0.76 rad and ≈1.52 rad at 532 nm and 1064 nm) rises in proportion to the wavelength increase. A similar result is obtained in the geometrical optics approximation [52,53]. Note that, according to the employed definition of an incident plane wave, see in Sec. III A, acquired phase shift $\delta\phi_1 = \arg[U_{\mathrm{scattered}}/U_{\mathrm{incident}}]$ is negative. In the phase representation the spreading of the object boundaries is barely visible. In contrast, in terms of the relative changes in the wave intensity the resultant diameter of the filament increases by ≈20% in the output plane because of wave diffraction occurring within the wave passage through the object. The brightness pattern of the plasma filament is

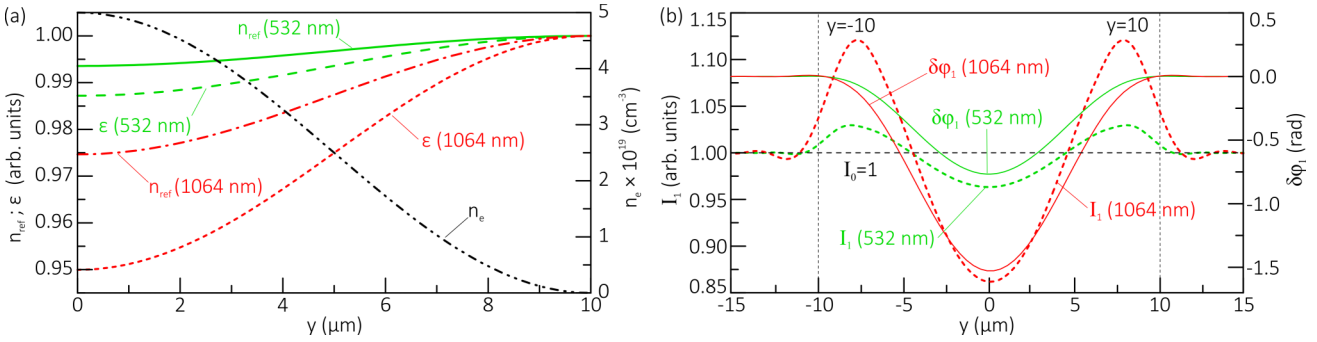

FIG. 2. Electron density n_e, dielectric permittivity ε, refractive index n_{ref} of a plasma filament 20 μm in diameter obtained at $\lambda = 532$ nm and $\lambda = 1064$ nm (a). Phase shift $\delta\phi_1(y)$ and intensity $I_1(y)$ of the diffracted wave (b) computed in the filament output plane ($x = 2R$) in the first Rytov approximation. Level $I_0 = 1$ corresponds to the incident plane wave intensity.

characterized by the decrease in the wave intensity at the object center and the increase in the intensity within the filament boundaries. The values of the corresponding changes at $\lambda = 532$ nm do not exceed 3.5% of the incident plane wave intensity ($I_0 = 1$), and become noticeable at longer wavelength (by ≈14% in the attenuation region and ≈12% in the enhancement region relative to unity). Thereinafter, we consider wave diffraction by plasma formations only in the first Rytov approximation, with the error being mainly driven by the discarded second term of the Rytov series, see Appendix B.

B. Diffracted wave in the near-field region

In Figs. 3 and 4 there are the diffraction maps and auxiliary panels illustrating the changes in intensity I and phase shift $\delta\phi$ of the propagating plane wave simulated behind the plasma filament (in its near-field region, at distances up to $L = 1$ mm), which is considered above. The parameter L stands for the distance between the filament output plane ($x = 2R$) and plane of interest behind the filament. The step of the computational grid in the longitudinal and transverse directions is 1 μm and 1 μm, respectively. It is seen that with increasing L the diffraction pattern of the filament significantly changes because of the diffraction spreading in free space. The amplitude of the intensity fluctuations, which are subtle at first glance in the filament output plane, rises sharply within 100 μm behind the filament. Herein alternating zones of local enhancement (maximum by ≈24% and ≈72% at $\lambda = 532$ nm and $\lambda = 1064$ nm) and attenuation (maximum by ≈30% and ≈70% at $\lambda = 532$ nm and $\lambda = 1064$ nm) of the wave intensity (relative to incident plane wave intensity $I_0 = 1$) are observed. The zones fit into a diffraction cone with an apex angle of about ≈19°

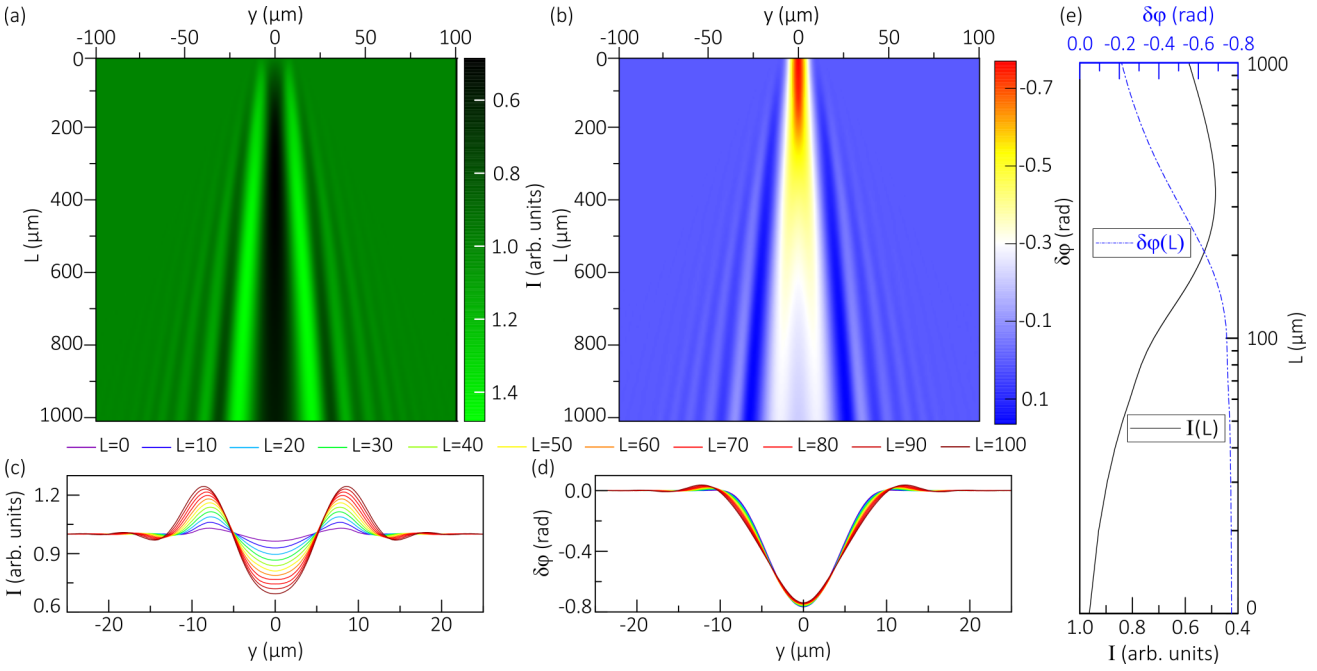

FIG. 3. Intensity (a) and phase shift (b) maps simulated (up to $L = 1000$ μm) for the wave with $\lambda = 532$ nm diffracted by the plasma filament 20 μm in diameter. Parameter L (μm) is the distance measured from the filament output plane ($x = 2R$). Intensity (c) and phase shift (d) profiles describe the wave diffraction in the periphery at distances up to $L = 100$ μm. Phase shift and intensity distributions (e) plotted along the wave propagation in the plane with the coordinate of $y = 0$.

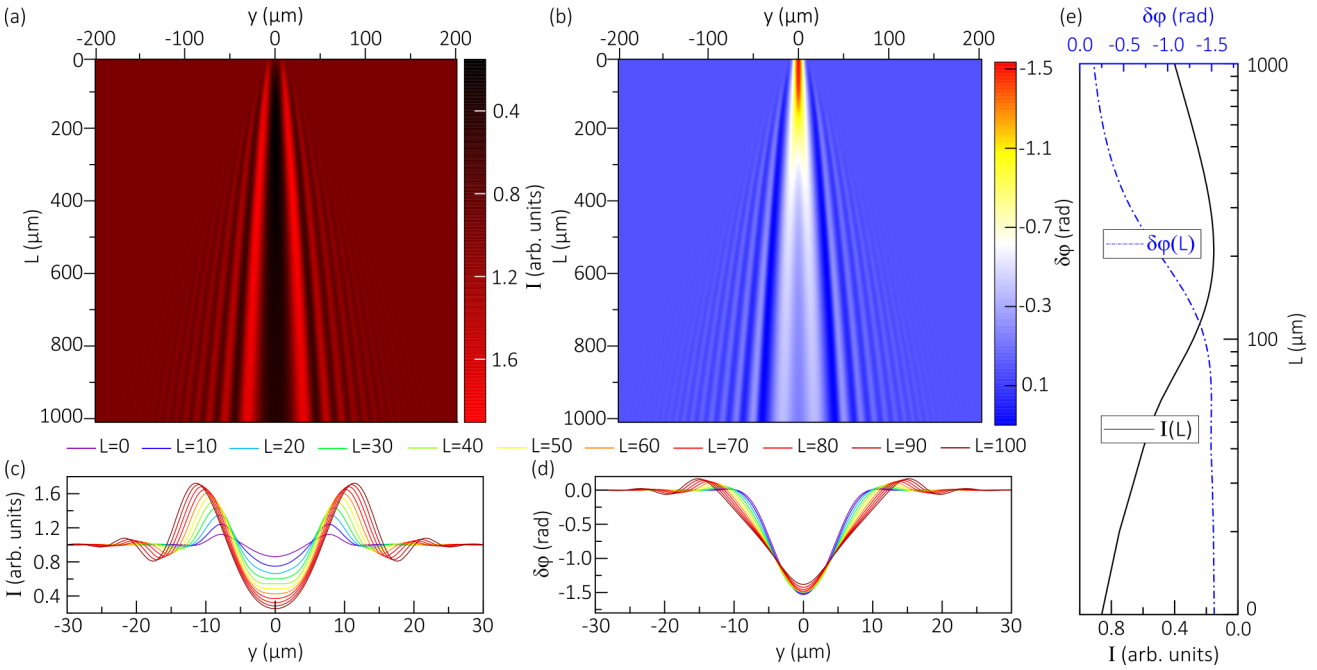

FIG. 4. Intensity (a) and phase shift (b) maps simulated (up to $L = 1000$ μm) for the wave with $\lambda = 1064$ nm diffracted by the plasma filament 20 μm in diameter. Parameter L (μm) is the distance measured from the filament output plane ($x = 2R$). Intensity (c) and phase shift (d) profiles describe the wave diffraction in the periphery at distances up to $L = 100$ μm. Phase shift and intensity distributions (e) plotted along the wave propagation in the plane with the coordinate of $y = 0$.

(at $\lambda = 532$ nm) and ≈24° (at $\lambda = 1064$ nm). The diffraction spreading significantly distorts the wave front in the periphery and entails the expansion of the filament boundaries even at the distances behind the filament of about 100 μm. This is the case for both the phase and brightness patterns of the filament. With respect to the incident plane wave intensity the most significant drop in the wave intensity is reached in the plane with the coordinate of $y = 0$, with the intensity drop being of approximately ≈52% at $L^* \sim 300$ μm for $\lambda = 532$ nm and ≈85% at $L^* \sim 200$ μm for $\lambda = 1064$ nm. Also, behind the filament at distances $L > 100$ μm the positive amplitude of the phase shift fluctuations gradually increases in the periphery, see the comments to this issue in Appendix C.

C. Influence of n_e^{max} on the enhancement of diffraction effects

Figure 5 shows the values of the maxima and minima for the phase shift, Fig. 5(a), and intensity, Fig. 5(b), of the diffracted wave in the filament output plane depending on maximum electron density n_e^{max}. Taking into account the symmetry of the filament and its fixed diameter, the phase shift and intensity profiles in the filament output plane reveal their similar behavior with respect to those calculated for different n_e^{max}. Only the values of the phase shift and intensity maxima and minima change, whereas these changes are linear in the framework of the first Rytov term and the negligible contribution of the second one. With a decrease in n_e^{max}

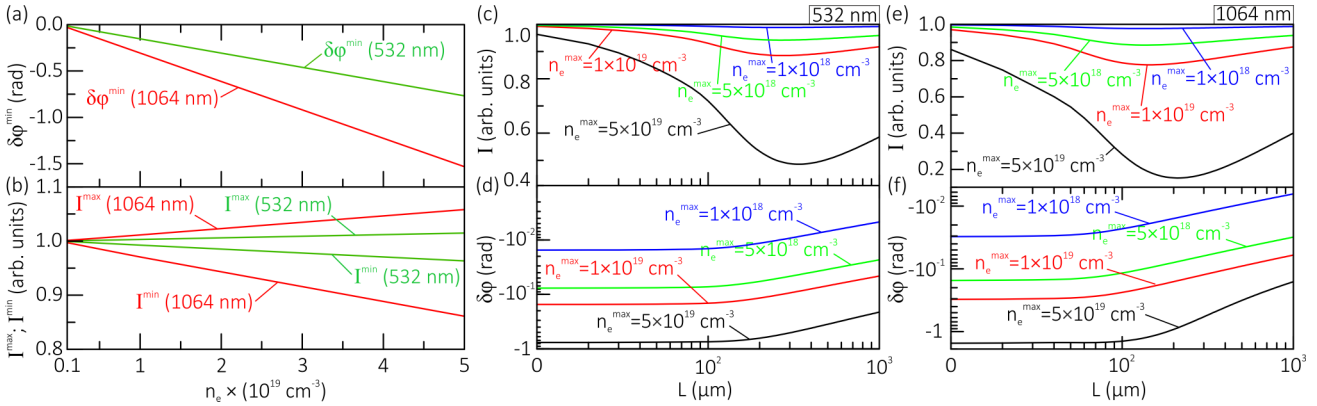

FIG. 5. Wave diffraction by a plasma filament 20 μm in diameter and different maximum electron densities n_e^{max}. Values of phase shift $\delta\phi^{min}$ (a) and intensity I^{max} and I^{min} (b) maxima and minima computed in the filament output plane ($x = 2R$) depending on n_e^{max}. Intensity (c), (e) and phase shift (d), (f) distributions constructed behind (up to $L = 1$ mm) the filament in the plane with the coordinate of $y = 0$; $\lambda = 532$ nm (c), (d) and $\lambda = 1064$ nm (e), (f) wavelengths are considered.

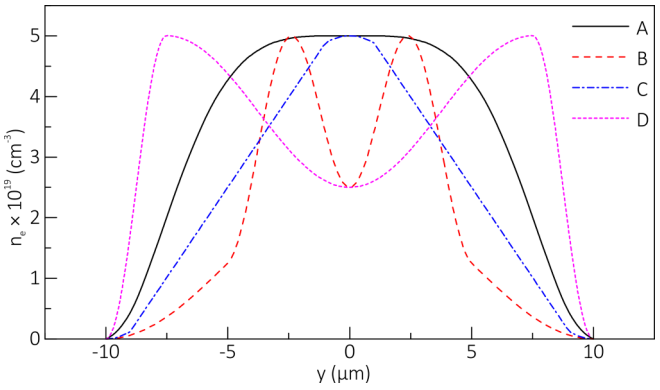

FIG. 6. Model profiles of the filament electron density.

from 5×10^{19} cm^{-3} to 10^{18} cm^{-3} the drop in the maximum changes in the phase shift and intensity reaches almost two orders of magnitude. In the output plane diffraction effects become insignificant already with $n_e^{\max} \approx 10^{19}$ cm^{-3} at $\lambda = 532$ nm and $n_e^{\max} \approx 5 \times 10^{18}$ cm^{-3} at $\lambda = 1064$ nm. At given $n_e^{\max}$ the changes in the phase shift and intensity do not exceed 2% for both wavelengths. So, as $n_e^{\max}$ decreases, diffraction effects in the filament output plane become weak. This fact correlates with the experimental observations pointing to vanishing diffraction effects in laser images of micron-sized plasma formations having a low electron density (no higher than $\sim 10^{17}$–10^{18} cm^{-3}). Behind the filament the diffraction effects naturally become strong, see Figs. 5(c)–5(f), but the resultant changes in the diffracted wave characteristics are in fact very weak for both wavelengths if electron densities are less than 10^{18} cm^{-3}.

D. Diffraction by plasma filaments with different electron density profiles

Real plasma formations can have nonhomogenous distributions of the electron density resulting in quite complex diffraction patterns. Let us consider such a case on the example of wave diffraction by plasma filaments with different electron density profiles in Fig. 6. Herein all selected profiles have equal $n_e^{\max} = 5 \times 10^{19}$ cm^{-3} and are defined in a 20 μm scale. The diffracted wave is presented in Fig. 7 in terms of the intensity and phase shift changes computed in the filament output plane. It is seen that even with sufficiently smooth curves of the phase shift the character of the intensity changes can be more sophisticated and accompanied by significant enhancements and attenuations of the intensity. A smooth increase in the electron density at the filament boundaries can lead to a less smooth distribution of the intensity (see distribution C). With a gradual change in the electron density around the filament center two characteristic minima instead of a single minimum can be observed (see distribution A). The tubular distributions (denoted as B and D) of the plasma electron density can entail the high-amplitude oscillations of the intensity in the filament output plane, although the phase shift curves remain smooth (see distribution B) or small fluctuations ("ears," see distribution D) manifest themselves around the filament center. Thus, as compared to the phase shift, the pattern of the intensity changes turns out to be the most sensitive to the small variations of the electron density distribution. This fact can be used when processing interferograms supplemented with the data obtained from shadowgrams.

E. Diffraction by plasma filaments with different diameters

Figure 8 shows the simulation results for plane wave diffraction by plasma filaments with equal maximum values ($n_e^{\max} = 5 \times 10^{19}$ cm^{-3}) of the electron density and similar profiles (similar to that in Sec. III A) but different diameters $2R$. Herein for each plasma filament and wavelength we plotted the intensity distributions in the filament output plane (the data are presented for half of the object pattern taking into account its symmetry), see Figs. 8(a) and 8(b), and constructed the intensity and phase shift distributions

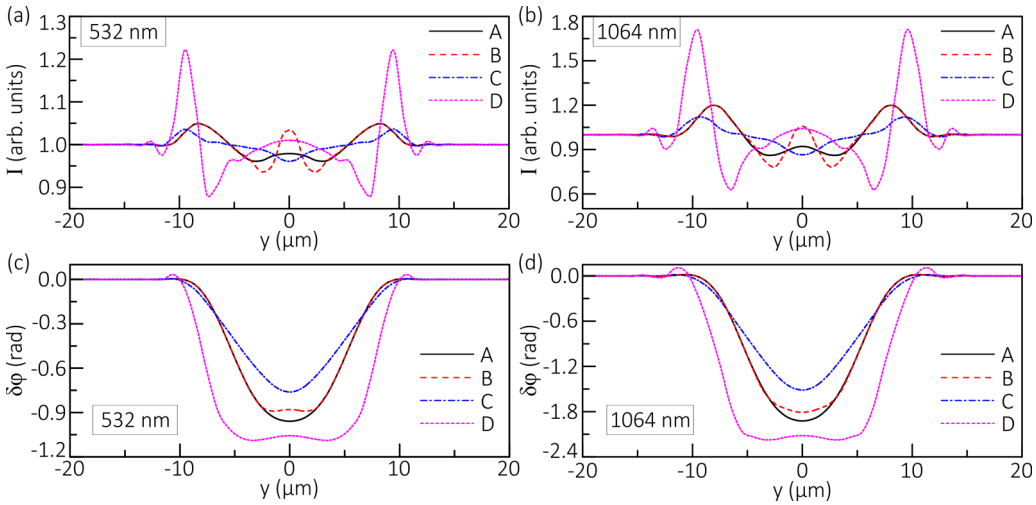

FIG. 7. Intensity (a), (b) and phase shift (c), (d) distributions computed in the output plane of the model plasma filaments with the electron density profiles in Fig. 6 for wavelengths $\lambda = 532$ nm (a), (c) and $\lambda = 1064$ nm (b), (d).

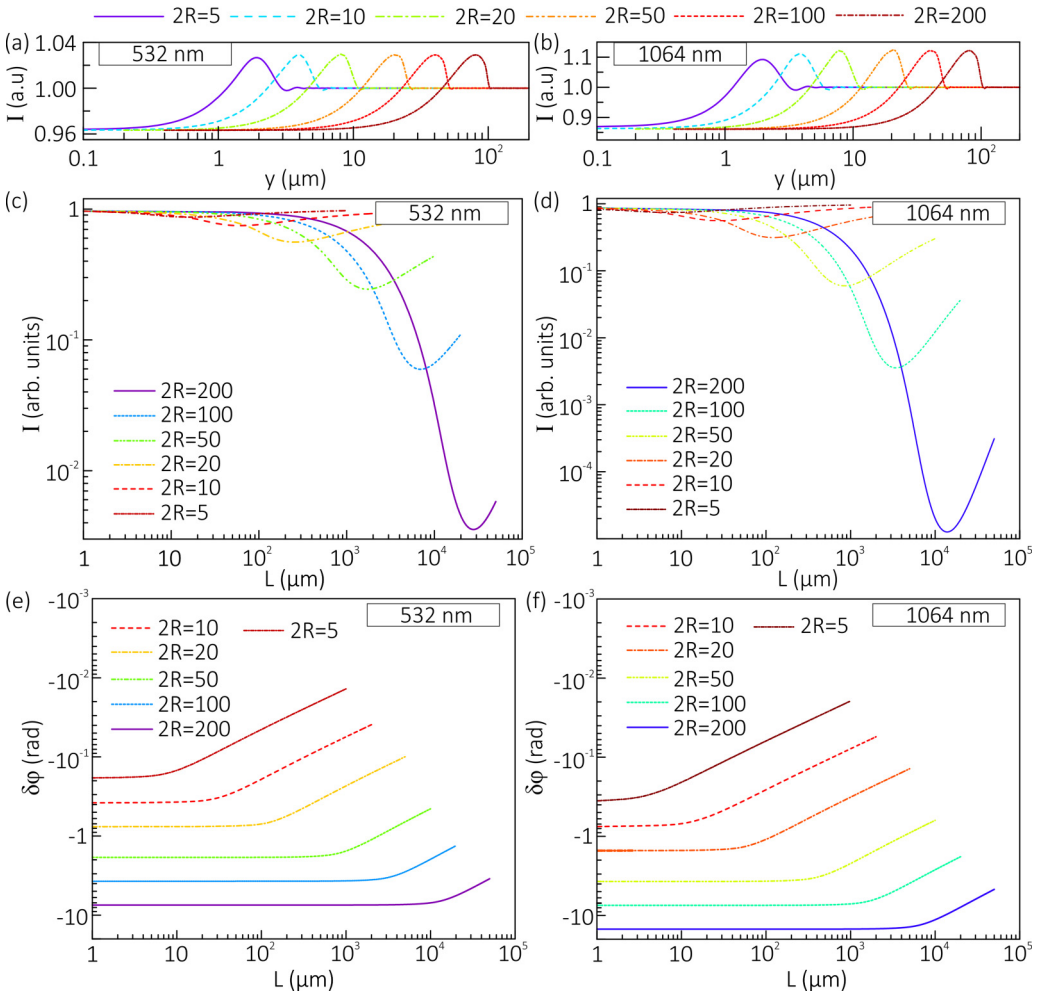

FIG. 8. Modeling results obtained for two wavelengths $\lambda = 532$ nm and $\lambda = 1064$ nm and plasma filaments with diameters $2R$: 5 μm, 10 μm, 20 μm, 50 μm, 100 μm, 200 μm. Intensity distributions (a), (b) in the filament output plane. Intensity (c), (d) and phase shift (e), (f) distributions along wave propagation in the plane with the coordinate of $y = 0$ calculated behind (up to $L = 10$ cm) the filaments.

along wave propagation in the plane with the coordinate of $y = 0$, see Figs. 8(c)–8(f). It is seen that the increase in the filament diameter does not change the values of the maxima and minima of the intensity fluctuations in the filament output plane. The shadow pattern only extends in the periphery as the object diameter increases. At the same time, the larger the filament diameter is, the more the intensity of the diffracted wave is disturbed in the near-field region. In this case the absolute value of the maximum phase shift also increases since the wave propagates in the plasma medium longer. As R increases, the region (L^*) with the maximum intensity attenuation shifts farther away from the filament, and the changes in the wave intensity become greater. In contrast, as R decreases, the closer to the filament output plane is the region (L^*) with the maximum intensity attenuation. The intensity changes become insignificant behind the filament as well. The diffraction patterns of all filaments remain similar, which displays only their scaling in space. This fact is important in achieving precise processing of the plasma images registered by optical lens systems with a defocusing effect.

IV. IMAGE FORMATION PROCESS IN A LENS SYSTEM: DEFOCUSING EFFECT

The diffraction theory described above is important to understand not only how a plasma formation is visualized in the field of coherent laser radiation, but also what its pattern looks like when it is registered by a lens optical system. Let us analyze this issue in detail and consider an optical system in the approximation of a single equivalent lens ("long-distance microscope") shown in Fig. 9(a).

This lens is focused on a thin metal electrode—wire 100 μm in diameter, approximately on its symmetry axis to obtain the wire image with a sharp boundary. Somewhere on the wire tip a small plasma formation appears, so that two cases of the lens focusing on this plasma object can be realized; see Figs. 9(b) and 9(c). Lens parameters: N.A. $= \sin\alpha = D/2d_0$ and N.A.$' = \sin\alpha' = D/2d_i$ are the input and output numerical apertures, D is the pupil diameter, and $M = d_i/d_0$ is the lens magnification. Distances d_0 and d_i are measured from the entrance and exit pupils to the object and image planes of the lens and obey thin-lens formula $1/d_0 + 1/d_i - 1/F = 0$,

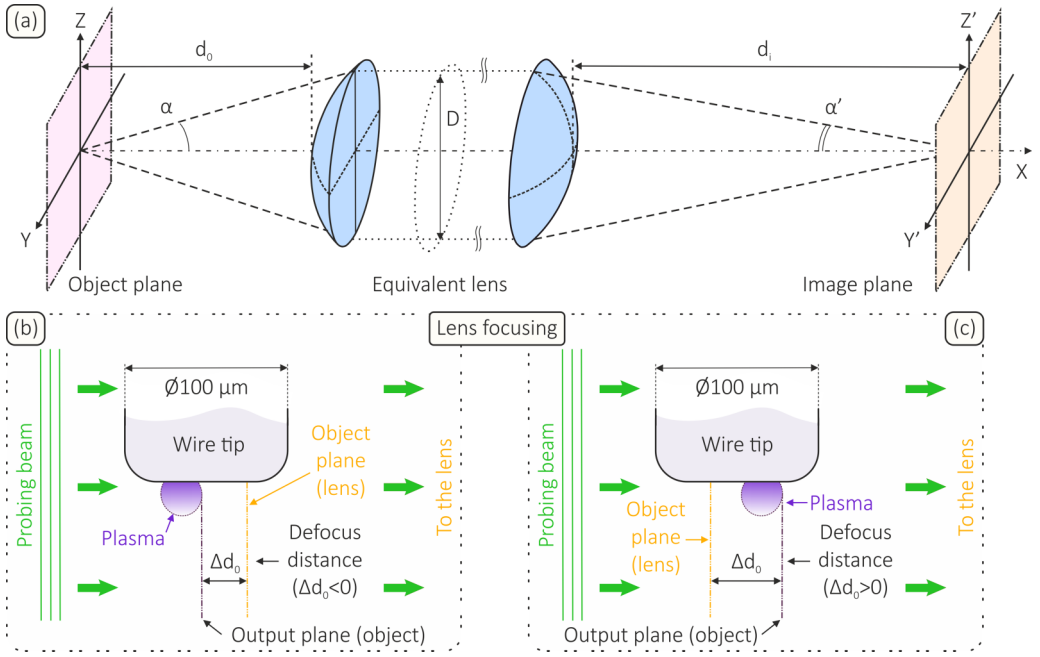

FIG. 9. Schematic representation of the equivalent single-lens system (a). Illustration of the lens focusing on the point electrode with a small plasma formation with a defocus distance: $\triangle d_0 < 0$—the lens object plane is behind the output plane of the plasma object (b), $\triangle d_0 > 0$—the lens object plane is in front of the output plane of the plasma object (c).

wherein F is the focal length. Let us turn to canonical object coordinates $\eta_y = -y\text{N.A.}/\lambda$ and $\eta_z = -z\text{N.A.}/\lambda$ and canonical image coordinates $\eta'_y = -y'\text{N.A.}'/\lambda$ and $\eta'_z = -z'\text{N.A.}'/\lambda$, which provide a onefold magnification and round pupil of a unit radius for the lens. With such coordinates and coherent illumination of the object the image formation process can be described in terms of the coherent transfer function of the optical system [51]

$$U_0(\rho_y, \rho_z) = \iint_{-\infty}^{+\infty} U_0(\eta_y, \eta_z) \times \exp\left(-2\pi \mathrm{i}[\eta_y\rho_y + \eta_z\rho_z]\right)\mathrm{d}\eta_y\eta_z, \quad (25)$$

$$U_i(\rho'_y, \rho'_z) = U_0(\rho_y, \rho_z)H(\rho_y, \rho_z), \quad (26)$$

$$U_i(\eta'_y, \eta'_z) = \iint_{-\infty}^{+\infty} U_i(\rho'_y, \rho'_z)\exp\left(2\pi \mathrm{i}[\eta'_y\rho'_y + \eta'_z\rho'_z]\right)\mathrm{d}\rho'_y\rho'_z, \quad (27)$$

$$H(\rho_y, \rho_z) = \begin{cases} \exp\left(2\pi \mathrm{i}W(\rho_y, \rho_z)\right), & \rho_y^2 + \rho_z^2 \leqslant 1, \\ 0, & \rho_y^2 + \rho_z^2 > 1. \end{cases} \quad (28)$$

Complex amplitudes $U_0(y, z)$ and $U_i(y', z')$ describe the wave diffracted by the plasma object in its output plane and the same wave in the image plane behind the lens. Function $H(\rho_y, \rho_z)$ appears as the generalized pupil function, which is obtained assuming no diffraction effects at the edges of the aperture diaphragm of the lens. Function $W(\rho_y, \rho_z)$ is the aberration function, which involves both the geometrical aberrations of the lens and the defocusing effect. We assume the geometrical aberrations to be negligible and associate $W(\rho_y, \rho_z)$ with the defocusing effect only.

The defocusing effect is that the lens object plane, when it is focused on the wire, may not coincide with the output plane of the plasma formation, wherein the object introduces the final changes in the characteristics of the transmitted wave. This is a natural situation for plasma, which can sporadically appear in experiments. Therefore, when imaging plasma, one should consider relative mismatch $\triangle d_0$ (defocus distance) between the object plane of the lens and the output plane of the plasma formation. The choice of the sign of $\triangle d_0$ is determined as follows. If the lens object plane coincides with the output plane of the plasma formation, then distance d_0 is optimal and we have $\triangle d_0 = 0$. In Fig. 9(b) the lens object plane is at a distance shorter than optimal d_0, and in terms of the relative changes in this distance we have $\triangle d_0 < 0$. In Fig. 9(c) the lens object plane, in contrast, is at a distance longer than optimal d_0, and we have $\triangle d_0 > 0$.

The defocusing effect in the object space (in front of the lens) naturally gives rise to a similar effect in the image space (behind the lens), which can be evaluated from relation $1/(d_0 + \triangle d_0) + 1/(d_i + \triangle d_i) - 1/F = 0$. Assuming that $M\triangle d_0/d_0 \ll 1$ (will be fulfilled in the experiment), we obtain $\triangle d_i \approx -M^2\triangle d_0$. The appearance of the defocusing effect in the image space naturally entails nonzero function $W(\rho_y, \rho_z)$ in the frequency response of the lens in Eq. (28), for which the following analytical expression can be derived [51,54]

$$W(\rho_y, \rho_z) = (2\lambda)^{-1}\text{N.A.}'^2\Delta d_i\left(\rho_y^2 + \rho_z^2\right). \quad (29)$$

Depending on the sign of defocus distance $\triangle d_0$ in the object space, $W(\rho_y, \rho_z)$ function takes positive or negative values.

Let us demonstrate the operation of the lens system on the example of imaging the plasma filament 20 μm in diameter, which is similar to that discussed in Sec. III A, in the presence of $\triangle d_0 < 0$ or >0. Here we consider only the case of $\lambda = 532$ nm. The corresponding results are shown in

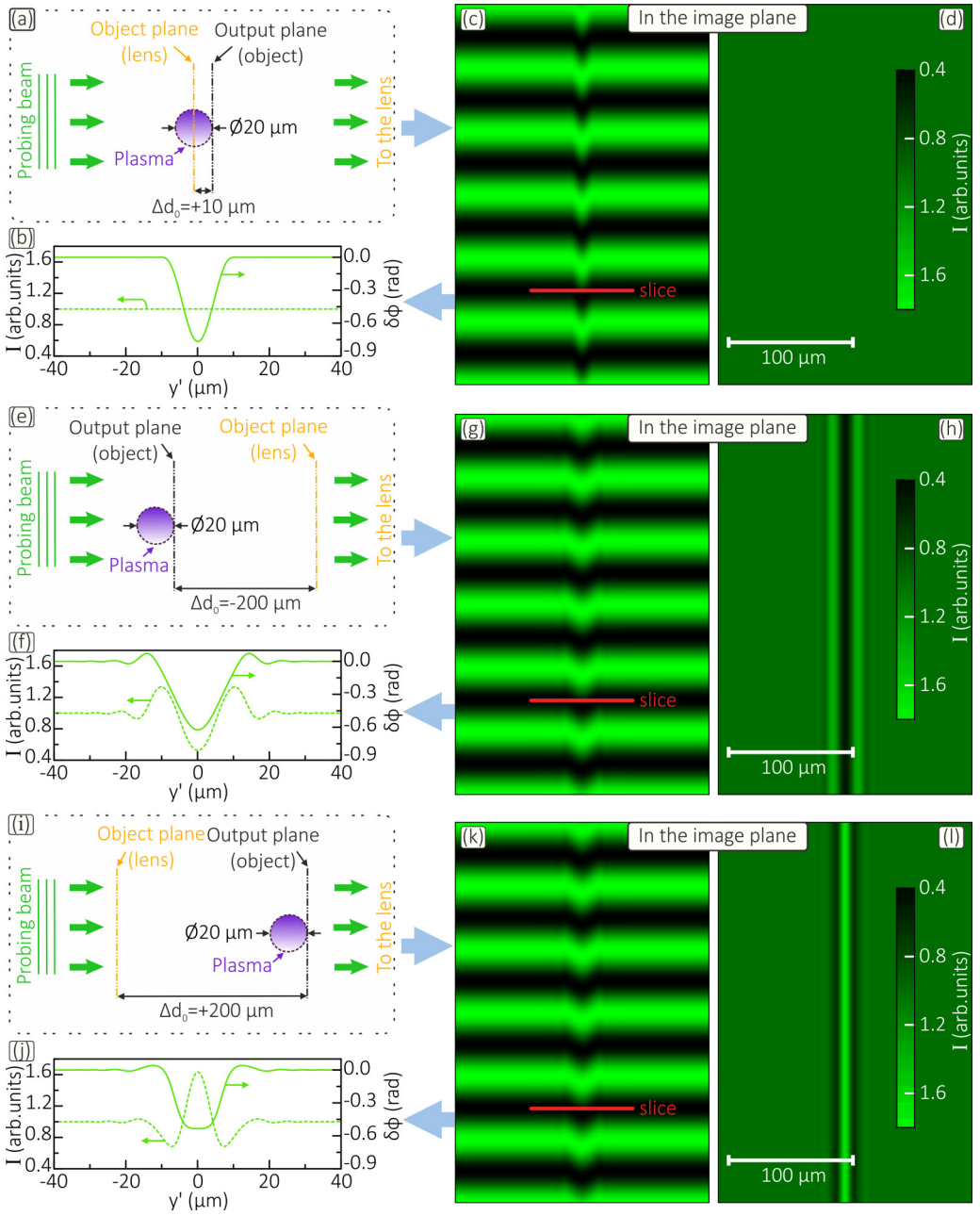

FIG. 10. (a)–(l) Visualization of a plasma filament 20 μm in diameter and 300 μm in length in the image plane of a lens (focal length 135 mm, relative number $f/2.8$, magnification 9.7) at $\lambda = 532$ nm. Relative to the filament output plane the lens object plane is focused: (a) on the geometric center of the filament ($\triangle d_0 = +10$ μm), (e) behind the filament ($\triangle d_0 = -200$ μm), (j) in front of the filament ($\triangle d_0 = +200$ μm). (b), (f), (j) Intensity and phase shift changes of the diffracted wave simulated in the lens image plane for $\triangle d_0 = +10$, -200, and $+200$ μm. (c), (g), (k) and (d), (h), (l) Simulated interferograms and shadowgrams of the filament in the image plane.

Fig. 10 and obtained by solving Eqs. (25)–(29). The lens has focal length $F = 135$ mm, relative number $f/2.8$, magnification $M = 9.7$ (values are taken similar to those discussed below in Sec. V A). It can be seen that, when the lens object plane is focused on the filament center (relative to the filament output plane with $\triangle d_0 = +10$ μm), see Fig. 10(a), the intensity fluctuations in the lens image plane disappear, see Fig. 10(b), and the filament phase pattern is recorded as correctly as possible, see the interferogram and shadowgram in Figs. 10(c) and 10(d). With $\triangle d_0 = -200$ μm, see Fig. 10(e), the filament diffraction pattern in the image plane, see Fig. 10(f), is no different from that shown in Fig. 3. Here one can distinguish the spreading of the phase shift profile, the appearance of the phase shift fluctuations of the opposite sign (regions wherein $\delta\phi > 0$), a drop in the image intensity in the object center (plane with the coordinate of $y = 0$), and an increase in the image intensity within the object periphery; see Figs. 10(g) and 10(h). With $\triangle d_0 = +200$ μm, see Fig. 10(i), in general, the filament phase pattern is similar to that observed with $\triangle d_0 = -200$ μm, but locally there are differences in the shapes of the phase shift profiles; see Fig. 10(j). The filament shadow pattern is inverted, i.e., one

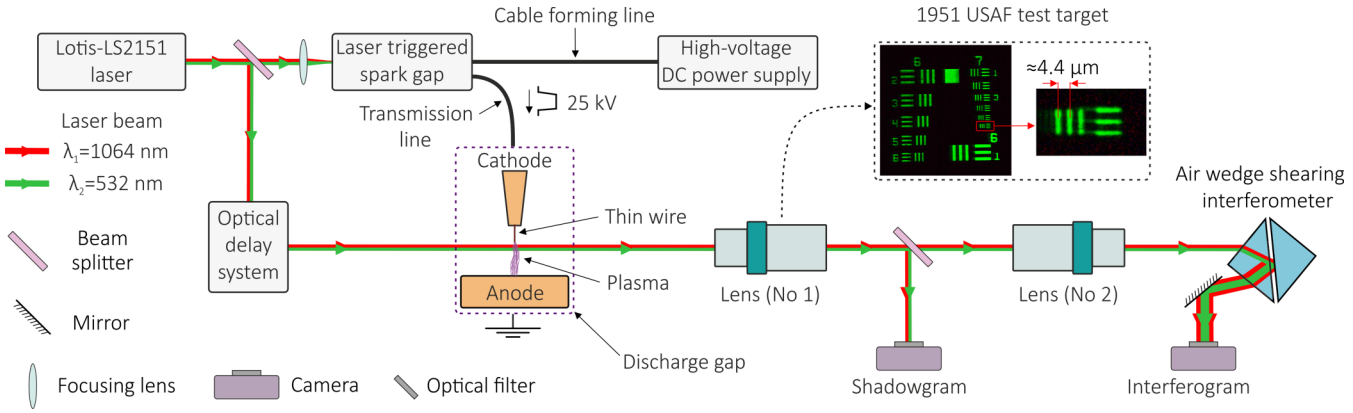

FIG. 11. Schematic representation of a diagnosing setup employed in imaging plasma microstructures at 532 nm and 1064 nm.

can observe an increase in the image intensity in the object center and its attenuation within the object periphery, see Figs. 10(k) and 10(l). Remarkably, the features of the image formation process in a lens system can be also explained in terms of forward ($\triangle x > 0$) and inverse ($\triangle x < 0$) propagation of the diffracted wave described by operator $P(\triangle x, f_\rho)$, see Appendix D.

V. EXPERIMENTAL VERIFICATION

A. Optical setup

It is important to verify the obtained numerical results employing the direct registration of the diffraction patterns of real plasma formations arising in the experiment. To this end, we developed a special diagnosing setup, the schematic representation of which is shown in Fig. 11. The setup was used in laser probing of near-cathode plasma, which appears during a nanosecond discharge in atmospheric air, and involved a picosecond Nd: YAG laser (Lotis LS-2151) with two wavelengths 1064 and 532 nm. A part of the output laser pulse (with both harmonics) was used to launch a laser-triggered spark gap [55]. When the breakdown of the spark gap occurs, a high-voltage generator (cable 75 Ω line charged by a high-voltage DC power supply up to 50 kV with negative polarity) produces a 25 kV pulse with the front of approximately 4 ns. The output pulse was supplied through the transmission line to the discharge chamber with the investigated discharge gap filled with atmospheric air, thereby provoking the discharge development. The other part of the laser pulse (low-divergence beam with a diameter of 2 cm) probes the investigated discharge gap. In a single shot laser radiation with only one wavelength was used when imaging plasma, which was provided by glass-optical filters placed in front of digital cameras. The transmitted laser radiation was collected by the first lens "Era-14" (focal length $F = 135$ mm, aperture number $f/2.8$) [56]. The image of the 1951 USAF test target in Fig. 11 was registered behind the first "Era-14" lens with 30× magnification and demonstrates a high spatial resolution of the lens at 532 nm, which is close to maximum theoretical resolution $l_{\max} \approx 0.61\lambda/\text{N.A.}^{\max} \approx 1.8$ μm, where $\text{N.A.}^{\max} \approx D/2F$. The object plane of the first lens was focused on approximately the symmetry axis of the cathode wire 100 μm in diameter to reach the wire sharp boundary in the images. The gap between the wire tip and opposite flat electrode (anode) was approximately 2 mm. Behind the first lens the laser beam was split into two beams, one of which was used in the channel with shadow imaging: direct registration of the beam intensity. The transmitted beam was collected by the second 'Era-14' lens and used to obtain interferograms. An air wedge shearing interferometer was used, with the wedge being placed approximately in the focal region of the second lens [57–59]. The laser shadowgram and interferogram were recorded by Canon EOS 1100D digital cameras (CMOS sensor 22.2 × 14.7 mm, 12.2 effective megapixels, removed IR cut-off filters) combined with glass-optical filters (also used to attenuate the discharge glow). During a single shot the camera shutters were opened by pressing a button; the shot took no more than 3 seconds. The resultant exposure time of the cameras was of the order of several seconds, but the discharge gap images themselves were obtained with a shorter exposure time. The latter was governed by the laser pulse duration, which constituted 100 ps at 1064 nm and 70 ps at 532 nm. The images were recorded with approximately 9.7× magnification.

B. Two wavelengths: Comparison of results

Figure 12 demonstrates laser shadowgrams, Figs. 12(a) and 12(b), and interferograms, Figs. 12(c) and 12(d), of plasma formations developing from the cathode tip in two independent shots. The images illustrate a key difference in the diffraction patterns of the plasma objects visualized at 1064 and 532 nm wavelengths. In Figs. 12(a) and 12(c) a plasma channel with a diameter of approximately 50 μm and a spot with a diameter of the order of 20 μm are observed. In Figs. 12(b) and 12(d) there is only a single plasma channel with a diameter of approximately 45 μm. The plasma patterns were obtained under similar conditions (when focusing the lens object plane on the cathode tip) and are characterized by an increase in the image intensity in the center of the objects and a decrease in the image intensity within the object boundaries. So, according to the intensity regularities and the way the plasma formations emerged at the surface of the cathode tip and started to develop in space, in both shots the plasma objects are imaged with $\triangle d_0 > 0$; see the illustrations in Figs. 9(c) and 10(i–l). For the observed plasma channels the changes in the radiation intensity relative to the image background are of the order of 25% at $\lambda = 532$ nm

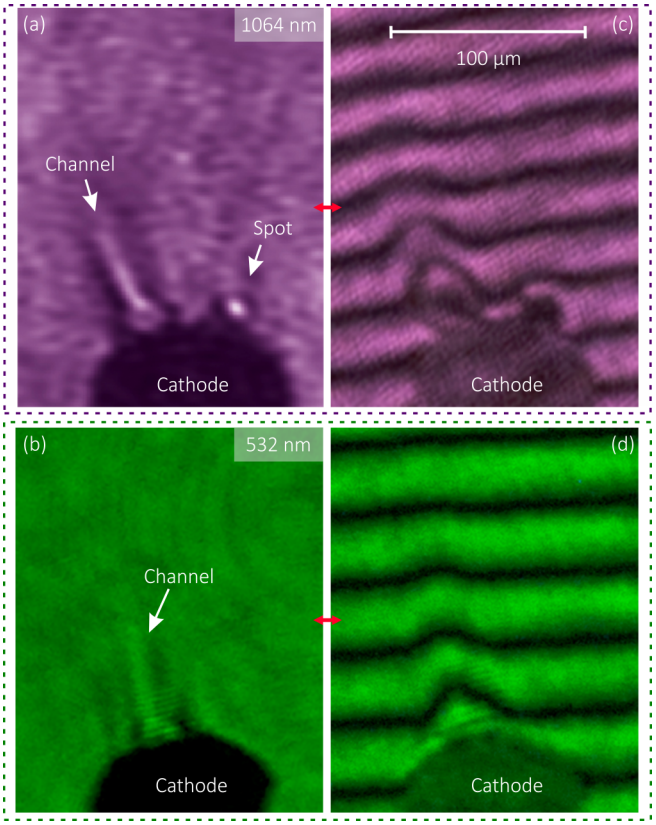

FIG. 12. Enlarged images of the near-cathode region: (a, b) shadowgrams and (c, d) interferograms obtained at 532 nm and 1064 nm approximately $\Delta t \approx 3.5$ ns after the gap breakdown.

and 50% at $\lambda = 1064$ nm. In the case of the cathode spot in Fig. 12(a), locally, the intensity enhancement reaches almost 100%, with the intensity attenuation being up to 50%. Proceeding from the numerical simulations, for the plasma channels in the images in Figs. 12(a) and 12(b) the defocus distance is expected to be of the order of several tens of micrometers. The plasma patterns themselves are characterized by an inhomogeneous intensity distribution, which is probably stipulated by the inhomogeneous and asymmetric distribution of the plasma electron density inside the objects. Nevertheless, the experimental data are consistent with the numerical results in Sec. III A, which predict the increase in the contrast of the plasma images when proceeding to a longer wavelength.

C. Invisibility in laser shadowgrams

In Sec. IV it was mentioned that, when the lens object plane is focused on approximately the center of a plasma object, the latter turns out to be invisible in laser shadowgrams, whereas the phase pattern is registered as correctly as possible. A real plasma object can have an asymmetrical and inhomogeneous distribution of the plasma electron density alongside with a certain inclination to the direction of the incident laser beam. However, one should expect a significant decrease in the object contrast in a laser shadowgram when the object center approximately coincides with the lens object plane. Let us demonstrate this fact on the example

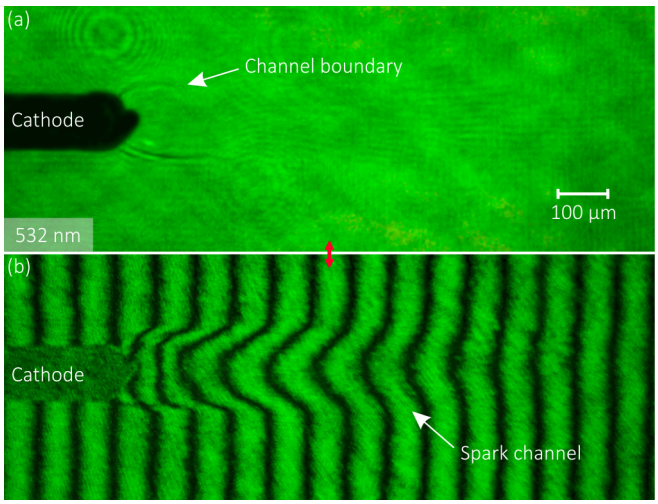

FIG. 13. Images of the spark channel developing from the cathode tip: (a) shadowgram and (b) interferogram obtained at 532 nm approximately $\Delta t \approx 7$ ns after the gap breakdown.

in Figs. 13(a) and 13(b). Here there are the shadowgram and interferogram of an extended spark channel (≈170 μm in diameter) developing from the tip of the point cathode (wire 100 μm in diameter). The images were obtained approximately 7 ns after the discharge gap breakdown. In this shot the lens object plane (equivalent of two lenses in Fig. 9) was focused on approximately the symmetry axis of the cathode wire. Moreover, in view of a big diameter of the channel in the near-cathode region one can assume that the lens object plane is focused almost on the symmetry center of the channel, even with the mismatch distance between the mentioned center and object plane being of the order of several tens of micrometers. The interference pattern in Fig. 13(b) has a high contrast, and the phase shift introduced by the plasma into the transmitted wave in the near-cathode zone corresponds to electron densities of about 3×19 cm^{-3}. To restore the electron density (in the first approximation), the classical inverse problem was considered in the framework of solving the inverted Abel integral equation [60]. At such high electron densities and with a certain defocus distance, one can in principle expect a high-contrast visualization of the spark channel in the shadowgram in Fig. 13(a), however, the channel is practically invisible far from the cathode. Only the channel boundaries near the cathode tip have a noticeable contrast; here the intensity attenuation reaches about 30% relative to the image background. Thus, both the object itself and its position relative to the object plane of the lens significantly affect the object visualization in laser shadowgrams.

D. Intensity inversion in laser shadowgrams

In special experiments we moved the camera back and forth in the optical channel with shadow imaging to trace the intensity inversion in laser shadowgrams. The corresponding results of imaging are shown in Fig. 14. Here there are shadowgrams of spark channels developing from the tip of the point cathode (wire 100 μm in diameter). The shadowgrams were registered at different instants after the gap breakdown. Two regimes of the object imaging were implemented. First,

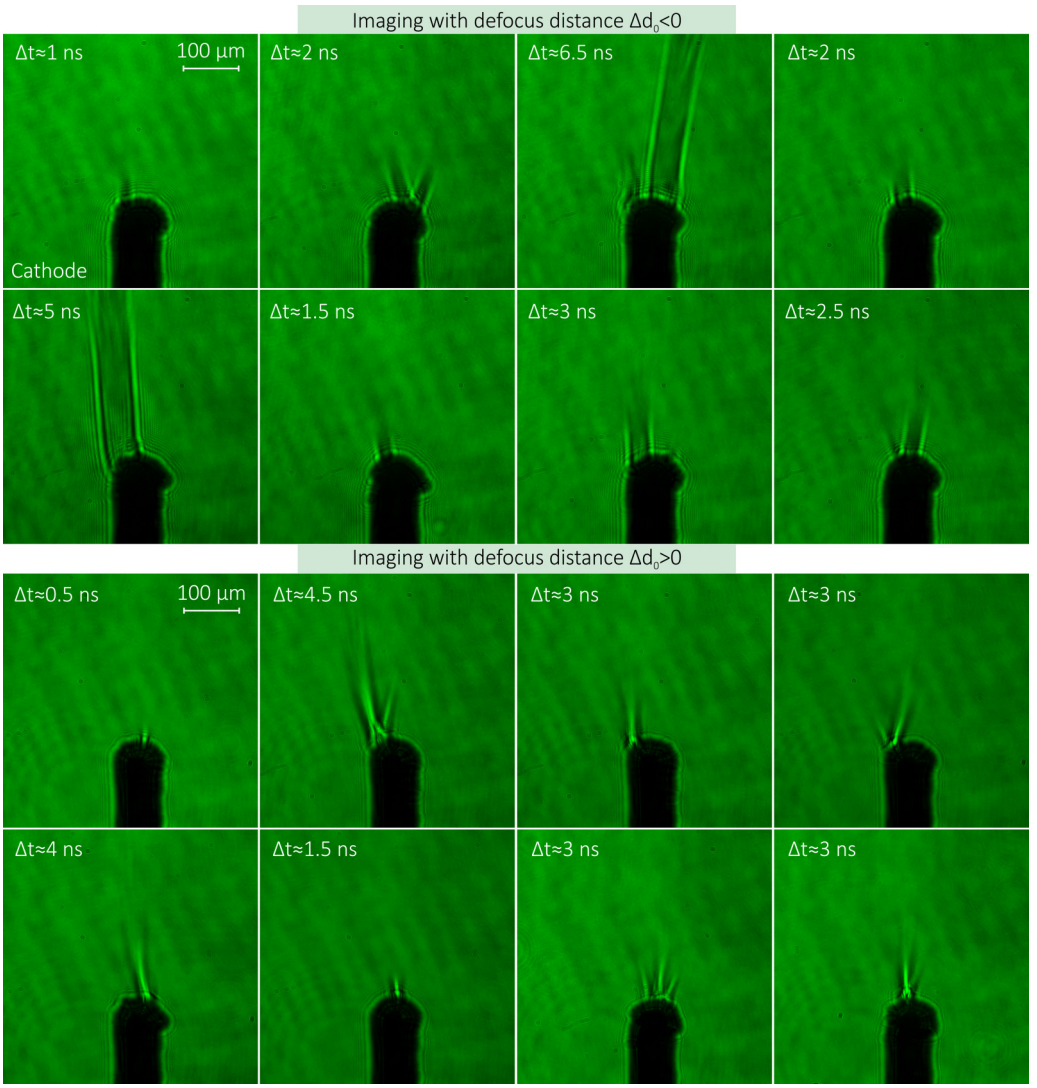

FIG. 14. Images of spark channels developing from the tip of the point cathode obtained with defocus distance $\triangle d_0 < 0$ and $\triangle d_0 > 0$ at different instants after $\triangle t$ the gap breakdown.

the lens object plane was focused on approximately the symmetry axis of the cathode wire to obtain its shadow image with a sharp boundary. Then, the camera in the optical channel with the shadow imaging was moved back and forth by approximately $\triangle d_i \approx +2$ cm and $\triangle d_i \approx -2$ cm, which corresponds to the shift of the lens object plane in the object space by approximately $\triangle d_0 \approx -200$ μm and $\triangle d_0 \approx +200$ μm, with the image magnification taken into account. It is seen that the images registered with $\triangle d_0 \approx -200$ μm are characterized by a significant attenuation of the image intensity in the object center and the intensity enhancement within the object periphery. This fact is consistent with the numerical results of calculating wave diffraction by model plasma filaments in Sec. III and the results of modeling the formation of the filament images in the optical system in Sec. IV. The asymmetry of the intensity distribution along the spark channels is driven by the inhomogeneity of the plasma electron density inside the channels. The images registered with $\triangle d_0 \approx +200$ μm, in contrast, are characterized by a significant enhancement of the image intensity in the object center and the intensity attenuation within the object periphery. This fact also agrees with the numerical results discussed in Sec. IV. In the laser shadowgrams, for both regimes of their registration with the used defocus distances, local attenuation and enhancement of the image intensity reach 70–80% on average, which is typical for plasma formations tens of micrometers in diameter having electron densities of $(1-5)\times 10^{19}$ cm^{-3}. Thus, the intensity inversion in laser shadowgrams, in fact, takes place in experiment and is well described by the developed diffraction theory supplemented with the theory of the plasma image formation in a lens system.

VI. DISCUSSION OF THE RESULTS

In the study we developed an efficient theory for analyzing the diffraction patterns of plasma microstructures, which are registered by lens systems in the presence of strong diffraction effects. Wave diffraction by plasma was evaluated by solving the scalar Helmholtz wave equation in the first Rytov approximation (see Sec. II B). This approximation is one of the asymptotic methods to describe wave diffraction in an inhomogeneous optical medium [1,3,49,61]. The

numerical simulation carried out in the framework of the first Rytov approximation has a number of advantages. Following this approximation, one can obtain computationally simple equation (20), which takes into account the diffraction spreading of the wave front as it passes through a plasma medium. Equation (20) also allows one to describe the propagation of the diffracted wave in free space, if restriction (12) is well fulfilled for the considered distances behind the object. We, however, circumvented this challenge by using spectral convolution (24) (see Sec. III C), which is beneficial for preserving all the information about the diffracted wave behind the object at long distances. The codes we developed to calculate wave diffraction by plasma microstructures were calibrated both on specific examples taken from experiments and on special numerical models, in which several independent calculation methods were employed simultaneously [53].

A key achievement of this work is that the comprehensive picture of wave diffraction by plasma microstructures was obtained in application to the plasma image processing. In particular we managed to explain the features of the plasma visualization (when plasma is considered as a purely phase object; see Sec. II A) in the field of coherent laser radiation. By varying the plasma electron density, the shape of its profile and the object diameter in Sec. III, we showed that the diffraction effects become stronger, the higher the electron density of the plasma object and the longer the wavelength of probing radiation are. Here it was surprising to discover that the object size does not influence the enhancement of the diffraction effects, see also in Ref. [53]. The diffraction effects are then enhanced behind the object in its near-field region. Due to this fact, in particular, the phase shift introduced by the object into the transmitted wave is distorted in terms of both the amplitude and shape. As a result, the areas with a phase shift of the opposite sign can appear in the object phase pattern, which, in turn, can be incorrectly associated in the experiment with the shock wave zone or the heated gas expanded from the plasma channel body to its shell, see also the comments in Appendix C. The presence of the electron density fluctuations inside the plasma object also entails the enhancement of the diffraction effects both in the object output plane and near-field region. In the case of the electron density fluctuations the diffraction effects significantly influence the formation of especially the shadow pattern of a complex-structured plasma object, see Sec. III D. The interpretation of such a pattern, when processing only the phase pattern of the object, turns out to be quite a difficult task.

Directly in the object output plane the changes in the intensity of the transmitted radiation can be insignificant, see Sec. III E. In the near-field region these changes, however, can reach very large values as the object diameter increases. Remarkably, as the object diameter increases, the resultant diffraction pattern scales, i.e., the changes in the intensity and phase shift of the diffracted wave rises in amplitude up to certain maximum values, which are reached at longer distances behind the object. At the same time, the distance behind the object, at which the object diffraction pattern is not greatly distorted because of the wave spreading, also increases in length. Owing to this fact, it becomes possible to correctly register (to some extent) the phase patterns of wide plasma objects even with a significant defocusing effect in a lens system, although this effect needs to be additionally controlled in experiments. It should be noted that the diffraction effects discussed above are enhanced with increasing the wavelength of probing radiation, whereas the distances behind the object, at which the most significant changes in the intensity and phase shift of the diffracted wave are achieved, become shorter.

Apart from the visualization mechanisms of plasma microstructures in the field of coherent laser radiation, we thoroughly analyzed the formation of their shadow and phase patterns, when the plasma is imaged by a lens system in the presence of the defocusing effect, see Sec. IV. This effect was shown to be easily explained in terms of the forward and inverse propagations of the diffracted wave in free space from the object output plane, see Sec. IV and in Appendix D. It is predicted that, depending on the adjustment of the lens object plane relative to the object output plane, one can observe the inversion of the regions with a significant attenuation and enhancement of the wave intensity within the object region in a laser shadowgram. Here an interesting effect is the invisibility of a plasma object or a sharp drop in the contrast of its shadow pattern in a laser shadowgram, when the lens object plane is focused on approximately the center of the object symmetry. In the case at hand, the phase pattern turns out to be localized directly in the object center, i.e., is registered as correctly as possible. Notably, the analysis of the shadow patterns of a plasma object registered in experiment in the presence of the defocusing effect in principle makes it possible to estimate the corresponding defocus distance and determine the relative position of the object output plane in space, even when a single angle of laser probing is employed. The analysis of the defocusing effect is also important for the reason that plasma can appear sporadically in experiment and evolve in space, thereby deviating over large distances from the position of the lens object plane.

The diffraction effects, which are predicted to be observed during the laser probing of plasma microstructures and visualized in the plasma images in a lens system, found their confirmation in experiments. To investigate the diffraction effects in detail, the special diagnosing setup based on laser probing techniques was developed, see Sec. V A. By using the setup, laser shadowgrams and interferograms of micrometer-sized cathode spots of plasma and spark channels (developing in atmospheric air after the discharge gap breakdown) were obtained, and the analysis of laser beam diffraction by these plasma objects was carried out, see Secs. V B–V D. The developed diffraction theory, while being combined with the image formation theory in a lens system, comprehensively explained the observed features of the shadow and phase patterns of real plasma objects. The knowledge of these features is important for the accurate reconstruction of the refractive index of the investigated plasma objects when solving the inverse diffraction problems. This issue we will discuss in detail in forthcoming publications.

Thus, our study can find broad applications in the processing of the laser images of different plasma microstructures registered by lens systems in the presence of strong diffraction effects. Note that the obtained findings are of a general nature and can be useful in evaluating laser diffraction also by

biological cells or tissues, turbulent gas and liquid flows, combustible gaseous mixtures, finely dispersed and condensed metastable media, etc.

VII. CONCLUSION

In the study we simulated diffraction of laser radiation by plasma filaments with smooth boundaries and micrometer-sized diameters (5–200 μm). The maximum electron densities (up to 5×10^{19} cm^{-3}) and the shape of their profiles were varied as well. The probing radiation was considered in the plane wave approximation for the wavelengths of 532 nm and 1064 nm. Wave diffraction was evaluated by solving the scalar Helmholtz wave equation in the first Rytov approximation supplemented with the spectral convolution, which involves the frequency operator describing the propagation of the wave angular spectrum in free space. In this manner we modeled the changes in the intensity and phase shift of the diffracted wave in the filament output plane and in the near-field region behind the filaments. Following a step by-step generalization of the picture of wave diffraction by plasma microstructures, we concerned the key diffraction effects, which accompany the laser beam transmission through inhomogeneous plasma. The employed diffraction theory was combined with the theory of the image formation of an object in a lens system, which made it possible to explain in detail the plasma visualization by optical systems in real experiments. A particular attention was laid on the defocusing effect governing the changes in the shadow and phase patterns of plasma. The discussed features of the plasma visualization, when laser probing is implemented, were found to rise in experiments and, thus, verified on example of laser probing of micrometer-sized plasma spots and spark channels emerging at the electrodes during a nanosecond air discharge. The consequences of the obtained results were discussed in application to processing of laser shadowgrams and interferograms of rapidly evolving plasma formations imaged by optical diagnostic systems.

ACKNOWLEDGMENT

The study was supported by the Russian Science Foundation (Grant No. 19-79-30086).

APPENDIX A: ILLUSTRATIONS OF PLASMA OBJECTS

A prime example of a plasma object, which is subject to the approximations made, is a thin filament of highly ionized plasma, see Figs. 15(a)–15(c). Such a filament, e.g., appears as an element of the complex internal microstructure of a resultant electric spark in a gas discharge, which was recently discovered in Refs. [25–28] by laser probing techniques. While being resulted from strong ionization and dissociation of the air medium, a plasma filament far from the electrodes has a characteristic diameter of about 10–20 μm and the plasma electron density in the filament center as high as $n_e \approx (1-5) \times 10^{19}$ cm^{-3} [26]. Maximum electron density $n_e = 5 \times 10^{19}$ cm^{-3} corresponds to the state of almost completely dissociated and singly ionized air under normal conditions. Note that the maximum electron density

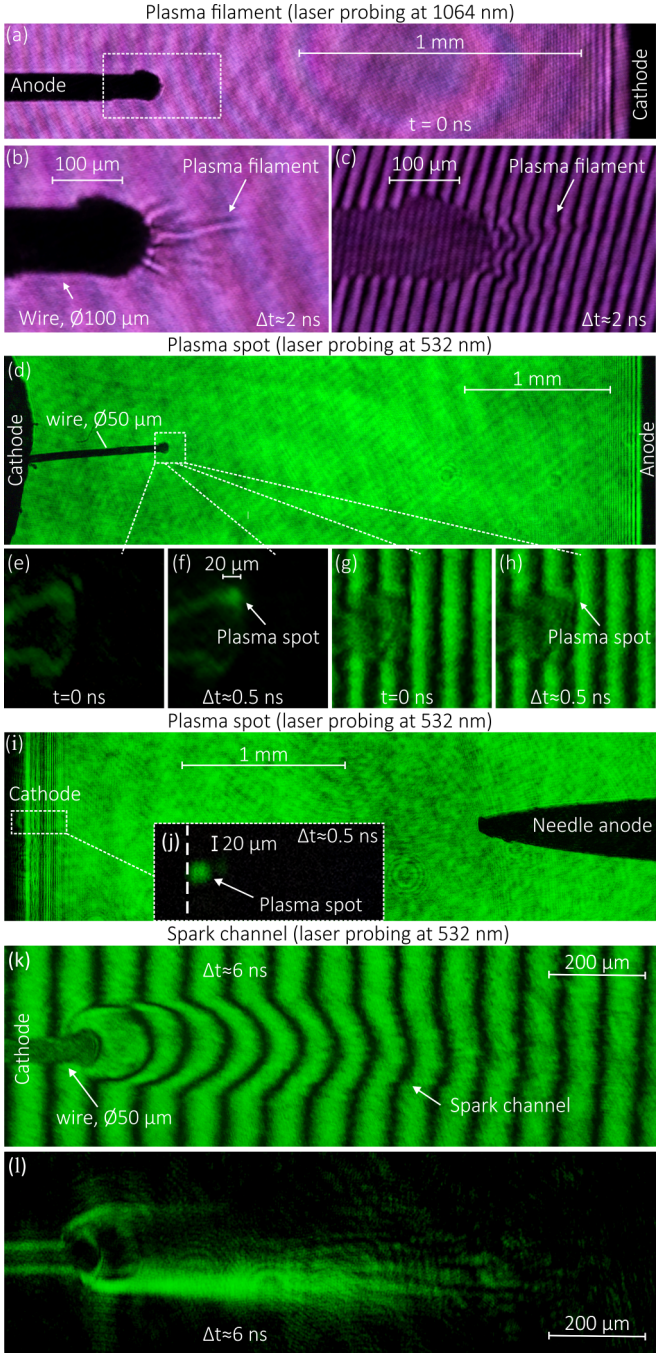

FIG. 15. Illustrative images of plasma formations. Plasma filament (a)–(c). (a) Shadowgram of the millimeter-sized air gap before ($t = 0$ ns) the discharge. (b) Shadowgram and (c) interferogram demonstrate the anode tip with plasma filaments formed $\Delta t \approx 2$ ns after the gap breakdown. Plasma spot (d)–(h). (d) Shadowgram of the millimeter-sized air gap before the discharge. (e), (f) Schlieren images and interferograms (g), (h) demonstrate the cathode tip before the discharge and when a micrometer-sized plasma spot forms $\Delta t \approx 0.5$ ns after the gap breakdown. Plasma spot (i), (j): (i) Shadowgram of the millimeter-sized air gap with the discharge; (j) Schlieren image of a micrometer-sized plasma spot obtained $\Delta t \approx 0.5$ ns after the gap breakdown. Spark channel (k), (l): (k) Interferogram; (l) Schlieren image of a spark channel developing from the point cathode.

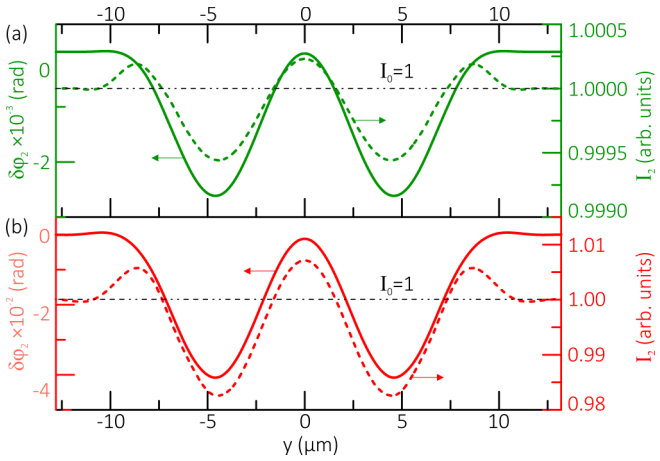

FIG. 16. Phase shift $\delta\phi_2(y)$ and intensity $I_2(y)$ of the diffracted wave in the filament output plane ($x = 2R$) computed for wavelengths $\lambda = 532$ nm (a) and $\lambda = 1064$ nm (b). The distributions are obtained from the second Rytov term. The level $I_0 = 1$ corresponds to the incident plane wave intensity.

of growing plasma channels is reached approximately at the center of their symmetry, which is a characteristic of highly ionized plasma often observed in experiments, although the mechanisms of its formation still remain the subject of intense research activity [65–70]. Having also a smooth boundary, a single filament can serve as a characteristic plasma inhomogeneity, with its parameters being similar to those of many plasma formations observed in experiments (see the plasma spots at the electrodes in Figs. 15(d)–15(h) and 15(i), 15(j) or the developing spark channel in Figs. 15(k), 15(l) imaged in the nanosecond discharge in atmospheric air). The illustrative images in Fig. 15 were obtained by employing the diagnosing setup discussed in Ref. [57].

The formations observed in Fig. 15 can be understood as the spatial regions occupied by plasma, which introduces the changes in the characteristics (phase shift, intensity, or more fundamentally, phase and group velocities) of the probing radiation because of the collective reaction of electrons oscillating around positively charged ions. The plasma images were obtained when probing with beams 70 ps (532 nm) and 100 ps (1064 nm) long, during which the movement of ions or neutral particles of the air medium can be neglected. The observed plasma formations appear, as a rule, after the instant of the discharge gap breakdown [41], when the discharge current rapidly grows up to several hundred amperes. In this case the magnetic fields arising around the plasma formations introduce a negligible contribution to the plasma dielectric permittivity, i.e., the plasma is unmagnetized. The formations were probed with laser beams having a diameter of about 1 cm and an energy of about 1 mJ, so there is no influence of the laser radiation on the plasma medium, and all the approximations used in Sec. II A are fulfilled. The same applies to the plasma formations considered in Sec. V.

APPENDIX B: BASIC ERROR OF COMPUTATION

Figure 16 shows phase shift $\delta\phi_2(y)$ and intensity $I_2(y)$ obtained from the second Rytov term. The distributions are also computed in the filament output plane for wavelengths $\lambda = 532$ nm and $\lambda = 1064$ nm. Functions $\delta\phi_2(y)$ and $I_2(y)$ have a similar behavior (excluding the edge effects). The absolute value of the maximum phase shift is $\delta\phi_2^{\max}(532\,\text{nm}) \approx 2.6 \times 10^{-3}$ rad and $\delta\phi_2^{\max}(1064\,\text{nm}) \approx 4.1 \times 10^{-2}$ rad, whereas $I_2(y)$ changes relative to the plane wave intensity no higher than 0.002% at $\lambda = 532$ nm and 2% at $\lambda = 1064$ nm. Proceeding from the distributions in Fig. 16, in the current study we restrict ourselves to the data ($\delta\phi \approx \delta\phi_1$ and $I \approx I_1$) obtained by computing the first Rytov term only. In this regard we expect the total computation error of the infinite Rytov series to be mainly driven by the discarded second term.

APPENDIX C: OPTICAL ARTIFACTS

Wave diffraction behind the filament results in the phase shift fluctuations having positive amplitude. This fact is crucial for precise image processing. Importantly, if the optical system is not well focused on the object, then the positive fluctuations of the phase shift in a laser interferogram can be visualized as a deflection of the interference fringes in the direction opposite to that in which the interference fringes would be shifted in the region filled with plasma. In the absence of *a priori* knowledge of the object properties such artifacts may be interpreted as a boundary region with refractive index $n > 1$. In other words, such a region can be considered as an increase in the density of neutral particles of the medium, which are expanded from the zone of the plasma formation because of their thermal expansion. The effect of this kind of the phase perturbations should be taken into account in experiments aimed at laser imaging of extended plasma channels [62–64] (imaged by a lens system with the mismatch from units to tens of centimeters between the lens object plane and the output plane of the considered phase object).

Finally, note that the observed fluctuations of the intensity and phase shift in the maps in Figs. 3 and 4 are stipulated only by diffraction of coherent laser radiation. From the physical point of view there is nothing contradictory. The energy of the diffracted wave is locally redistributed in the periphery, whereas the total energy remains constant.

APPENDIX D: OBJECT VISUALIZATION

The simulated filament images in the lens image plane in Fig. 10 can be considered as those in the lens object plane, which have undergone spatial high-pass filtering. Let us assume that the lens spatial resolution allows one to register all the significant details (primarily those that are small) of the object. Then the object images in the image plane can be directly associated with the object patterns in the object space (in front of the lens), which are obtained when computing wave diffraction for its forward and inverse directions of propagation (in free space) from the object output plane. In both cases wave propagation from the object output plane to the lens object plane can be described using convolution $\mathcal{F}(U(x + \Delta x, \rho)) = \mathcal{F}(U(x, \rho)) \times P(\Delta x, f_\rho)$, wherein $P(\Delta x, f_\rho) = \exp[2\pi i \Delta x(\lambda^{-2} - f_\rho^2)^{1/2}]$ and $\Delta x > 0$ or $\Delta x < 0$ depending on the considered situation;

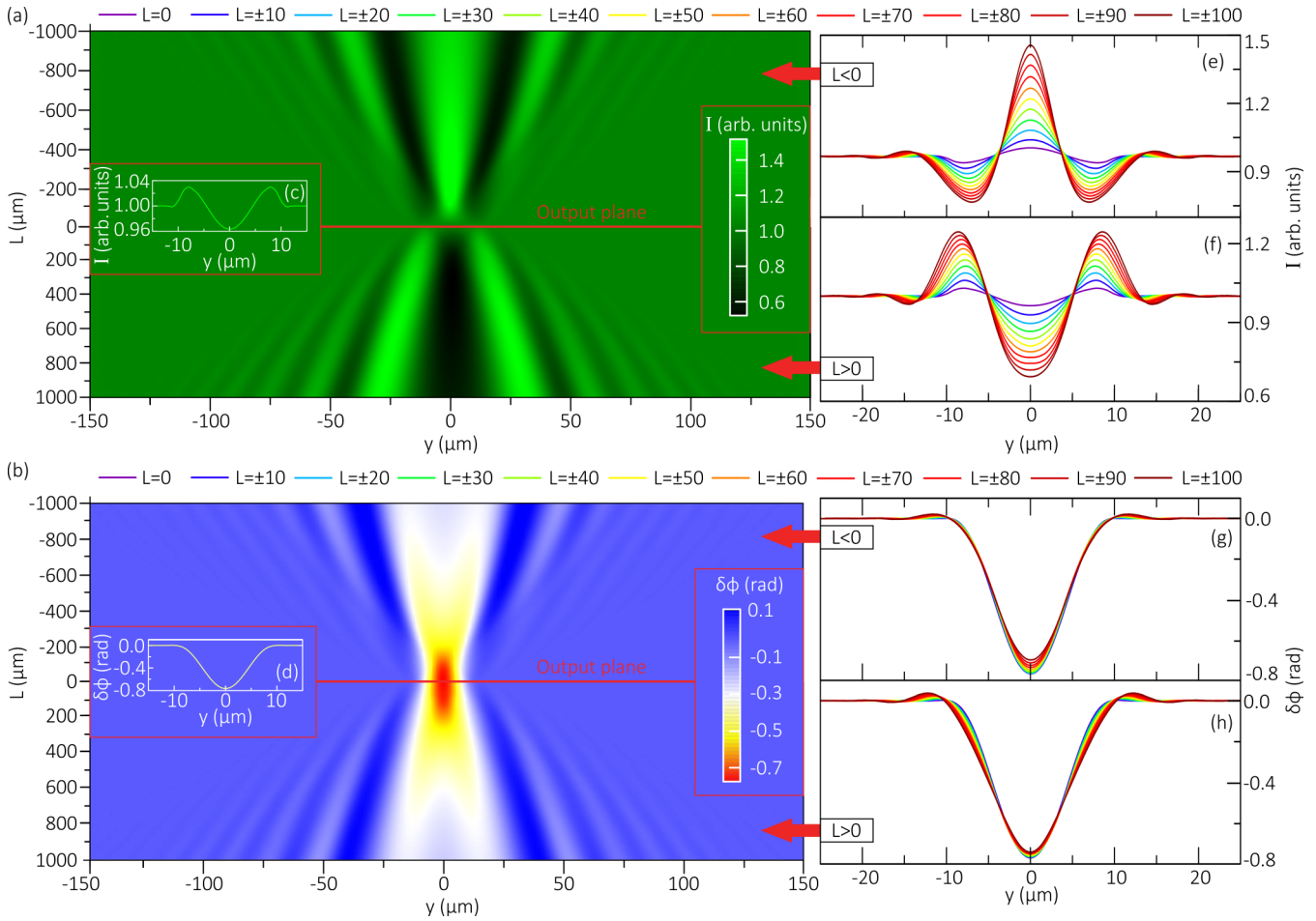

FIG. 17. Maps demonstrating the relative changes in the intensity (a) and phase shift (b) of the diffracted wave (with $\lambda = 532$ nm) obtained for its forward and inverse directions of propagation from the filament output plane (filament is 20 μm in diameter). The intensity (c) and phase shift (d) distributions are simulated for the filament output plane. The distributions (e), (f) and (g), (h) describe the wave characteristics for the inverse (e), (g) and forward (f), (h) directions of wave propagation. The parameter L (μm) is the distance between the filament output plane and plane considered behind ($L > 0$) or in front of ($L < 0$) the filament.

see Figs. 9(b) or 9(c). Let us demonstrate the relationship between the filament diffraction patterns in Fig. 10, which are registered by the lens, and those in Fig. 17 obtained by computing the propagation of the wave angular spectrum for $\triangle x > 0$ and $\triangle x < 0$.

In Figs. 17(a) and 17(b) there are the maps demonstrating the relative changes in the intensity and phase shift of the diffracted wave (with the wavelength of 532 nm) obtained for its forward and inverse directions of propagation from the filament output plane (for distances L up to $+1$ mm and -1 mm). The filament (20 μm in diameter) is taken similar to that considered in Sec. III A. The wave characteristics in the filament output plane are shown in Figs. 17(c) and 17(d), and their changes in free space are demonstrated in Figs. 17(e)–17(h). The diffraction pattern obtained with $L > 0$ is identical to that in Fig. 3. So, let us discuss in detail the diffraction pattern obtained for the inverse direction of wave propagation. Here most of the diffracted wave energy is also concentrated in the diffraction cone with an apex angle of $\approx 19^\circ$ at $\lambda = 532$ nm. The positive and negative oscillations of the phase shift are similar in both cases of wave propagation, see Figs. 17(g) and 17(h), but the intensity fluctuations are inverted, see Figs. 17(e) and 17(f). The former zones (obtained with $L > 0$) with the intensity attenuation become the zones (obtained with $L < 0$) with the intensity enhancement. For example, the diffraction pattern of the filament obtained for the forward direction of wave propagation is characterized by a significant attenuation of the wave intensity in the plane with the coordinate of $y = 0$. With the inverse direction of wave propagation, in contrast, in such a plane the filament pattern is characterized by a significant increase in the wave intensity. Directly in the center of the object (with the inverse direction of wave propagation in the plane with the coordinate of $L = -10$ μm on the Ox axis) its brightness pattern disappears (object becomes invisible), whereas the phase shift reaches its resultant minimum (phase pattern turns out to be localized in the object center). Such a wave behavior is a characteristic of symmetrical objects. For other objects the resultant diffraction pattern appears to be quite complicated, but the fundamental essence, e.g., associated with the intensity inversion, remains the same. Notably, the phase shifts in the center of the object and in its output plane differ by no more than 1%, and, owing to the high spatial resolution of the lens, the profiles of the intensity and phase shift of the diffracted

wave in the maps in Fig. 17 almost completely coincide with those presented in Fig. 10 for the corresponding values of $\triangle d_0$.

Thus, each resultant diffraction pattern in Figs. 17(a) and 17(b) obtained in terms of the intensity or phase shift changes for both cases of wave propagation appears as the two opposite-directed diffraction cones with a special narrow zone between them, wherein there are particular regularities in the behavior of the wave characteristics. Remarkably, the knowledge of these regularities allows one to estimate the defocus distance together with the position of the object output plane in space even when a single angle of laser probing is employed. Finally, note that the simulation results in Fig. 17 are in a good agreement with those in Fig. 10, which are obtained by using the theory of the image formation of a phase object in a lens system in the presence of the defocusing effect. In other words, the maps in Figs. 17(a) and 17(b) are nothing more than the filament patterns, which can be observed through a lens system. In particular, the wave intensity attenuation in the plane with the coordinate of $y = 0$ behind the filament is consistent with the modeling results in Figs. 10(e) and 10(f). The wave intensity enhancement in such a plane with the inverse direction of wave propagation agrees with the results in Figs. 10(i) and 10(j).

[1] D. L. Marks, A family of approximations spanning the Born and Rytov scattering series, Opt. Express **14**, 8837 (2006).

[2] Y. Sung, W. Choi, C. Fang-Yen, K. Badizadegan, R. R. Dasari, and M. S. Feld, Optical diffraction tomography for high resolution live cell imaging, Opt. Express **17**, 266 (2009).

[3] P. Müller, M. Schürmann, and J. Guck, The theory of diffraction tomography, arXiv:1507.00466.

[4] S. I. Knizhin, Using spatial radio wave field processing for diagnostics of inhomogeneous plasma, Waves Random Complex Media **31**, 2115 (2021).

[5] *Plasma Diagnostic Techniques*, edited by R. H. Huddlestone and S. L. Leonard (Academic Press, New York, 1965).

[6] L. A. Vasilev, *Schlieren Methods* (Israel Program, New York, 1971).

[7] U. Kogelschatz and W. Schneider, Quantitative Schlieren techniques applied to high current arc investigations, Appl. Opt. **11**, 1822 (1972).

[8] G. S. Settles, *Schlieren and Shadowgraph Techniques: Visualizing Phenomena in Transparent Media* (Springer Science & Business Media, Berlin, 2001).

[9] L. A. Gizzi, M. Galimberti, A. Giulietti, D. Giulietti, P. Koester, L. Labate, P. Tomassini, P. Martin, T. Ceccotti, P. De Oliveira, and P. Monot, Femtosecond interferometry of propagation of a laminar ionization front in a gas, Phys. Rev. E **74**, 036403 (2006).

[10] A. J. Gonsalves, T. P. Rowlands-Rees, B. H. P. Broks, J. J. A. M. van der Mullen, and S. M. Hooker, Transverse interferometry of a hydrogen-filled capillary discharge waveguide, Phys. Rev. Lett. **98**, 025002 (2007).

[11] G. Ostrovskaya, Holographic diagnostics of the plasma: A review, Tech. Phys. **53**, 1103 (2008).

[12] P. K. Panigrahi and K. Muralidhar, *Schlieren and Shadowgraph Methods in Heat and Mass Transfer* (Springer, Berlin, 2012), Vol. 2.

[13] H. Quevedo, M. McCormick, M. Wisher, R. D. Bengtson, and T. Ditmire, Simultaneous streak and frame interferometry for electron density measurements of laser produced plasmas, Rev. Sci. Instrum. **87**, 013107 (2016).

[14] V. P. Silin, Absorption of radiation by turbulent laser plasmas, Sov. Phys. Usp. **28**, 136 (1985).

[15] M. Mahdavi and S. Ghazizadeh, Linear absorption mechanisms in laser plasma interactions, J. Appl. Sci. **12**, 12 (2012).

[16] T. Yong, A. Abdalla, and M. Cappelli, Laser absorption measurements of electron density in nanosecond-scale atmospheric pressure pulsed plasmas, Phys. Plasmas **28**, 053501 (2021).

[17] E. Parkevich, M. Medvedev, A. Khirianova, G. Ivanenkov, A. Agafonov, A. Selyukov, A. Mingaleev, T. Shelkovenko, and S. Pikuz, Investigation of a near-electrode plasma formed in the atmospheric discharge with employment of picosecond laser probing, J. Russ. Laser Res. **40**, 56 (2019).

[18] C. Haas, G. Pretzier, and H. Jäger, Determination of particle densities and line profiles in plasmas by resonance interferometry: A feasibility study using computer simulated refractivity data, Z. Naturforsch. A **50**, 902 (1995).

[19] C. Joshi, The nonlinear optics of plasmas, Phys. Scr. **1990**, 90 (1990).

[20] R. Lehmberg and J. Stamper, Depolarization in laser probing of inhomogeneous magnetized plasmas, Phys. Fluids **21**, 814 (1978).

[21] T. Pisarczyk, A. Rupasov, G. Sarkisov, and A. Shikanov, Faraday-rotation method for magnetic-field diagnostics in a laser plasma, J. Sov. Laser Res. **11**, 1 (1990).

[22] R. Han, C. Li, W. Yuan, J. Ouyang, J. Wu, Y. Wang, W. Ding, and Y. Zhang, Experiments on plasma dynamics of electrical wire explosion in air, High Voltage **7**, 117 (2022).

[23] S. N. Kolgatin, M. L. Lev, B. P. Peregud, A. M. Stepanov, T. A. Fedorova, A. S. Furman, and A. V. Khachatur'yants, Destruction of copper wire by the passage of currents with densities above 10^7 A/cm^2, Žh. Tekh. Fiz. **59**, 123 (1989).

[24] V. Romanova, G. Ivanenkov, E. Parkevich, I. Tilikin, M. Medvedev, T. Shelkovenko, S. Pikuz, and A. Selyukov, Laser scattering by submicron droplets formed during the electrical explosion of thin metal wires, J. Phys. D **54**, 175201 (2021).

[25] E. Parkevich, M. Medvedev, A. Khirianova, G. Ivanenkov, A. Selyukov, A. Agafonov, K. Shpakov, and A. Oginov, Extremely fast formation of anode spots in an atmospheric discharge points to a fundamental ultrafast breakdown mechanism, Plasma Sources Sci. Technol. **28**, 125007 (2019).

[26] E. Parkevich, M. Medvedev, G. Ivanenkov, A. Khirianova, A. Selyukov, A. Agafonov, P. A. Korneev, S. Gus'kov, and A. Mingaleev, Fast fine-scale spark filamentation and its effect on the spark resistance, Plasma Sources Sci. Technol. **28**, 095003 (2019).

[27] K. Almazova, A. Belonogov, V. Borovkov, V. Kurbanismailov, Z. Khalikova, P. K. Omarova, G. Ragimkhanov, D. Tereshonok, and A. Trenkin, Investigation of the microchannel structure in the initial phase of the discharge in air at atmospheric pressure in the "pin (anode)-plane" gap, Phys. Plasmas **27**, 123507 (2020).

[28] K. I. Almazova, A. N. Belonogov, V. V. Borovkov, V. S. Kurbanismailov, G. B. Ragimkhanov, A. A. Tren'kin, D. V. Tereshonok, and Z. R. Khalikova, Plasma and gas-dynamic near-electrode processes in the initial phase of a microstructured spark discharge in air, Tech. Phys. Lett. **46**, 737 (2020).

[29] A. Khirianova, E. Parkevich, M. Medvedev, K. Smaznova, T. Khirianov, E. Varaksina, and A. Selyukov, Extraction of high-contrast diffraction patterns of fine-structured electrical sparks from laser shadowgrams, Opt. Express **29**, 14941 (2021).

[30] L. Soto, C. Pavez, F. Castillo, F. Veloso, J. Moreno, and S. Auluck, Filamentary structures in dense plasma focus: Current filaments or vortex filaments? Phys. Plasmas **21**, 072702 (2014).

[31] S. Polukhin, A. Gurei, V. Y. Nikulin, E. Peregudova, and P. Silin, Studying how plasma jets are generated in a plasma focus, Plasma Phys. Rep. **46**, 127 (2020).

[32] G. V. Ostrovskaya *et al.*, Laser spark in gases, Sov. Phys. Usp. **16**, 834 (1974).

[33] Y. Ping, I. Geltner, A. Morozov, and S. Suckewer, Interferometric measurements of plasma density in microcapillaries and laser sparks, Phys. Plasmas **9**, 4756 (2002).

[34] W. Wei, X. Li, J. Wu, Z. Yang, S. Jia, and A. Qiu, Interferometric and Schlieren characterization of the plasmas and shock wave dynamics during laser-triggered discharge in atmospheric air, Phys. Plasmas **21**, 083112 (2014).

[35] Z. Yang, W. Wei, J. Han, J. Wu, X. Li, and S. Jia, Experimental study of the behavior of two laser produced plasmas in air, Phys. Plasmas **22**, 073511 (2015).

[36] S. S. Mao, X. Mao, R. Greif, and R. E. Russo, Initiation of an early-stage plasma during picosecond laser ablation of solids, Appl. Phys. Lett. **77**, 2464 (2000).

[37] S. S. Mao, X. Mao, R. Greif, and R. E. Russo, Influence of preformed shock wave on the development of picosecond laser ablation plasma, J. Appl. Phys. **89**, 4096 (2001).

[38] P. Nicolaï, C. Stenz, A. Kasperczuk, T. Pisarczyk, D. Klir, L. Juha, E. Krousky, K. Masek, M. Pfeifer, K. Rohlena *et al.*, Studies of supersonic, radiative plasma jet interaction with gases at the prague asterix laser system facility, Phys. Plasmas **15**, 082701 (2008).

[39] S. Harilal, G. Miloshevsky, P. Diwakar, N. LaHaye, and A. Hassanein, Experimental and computational study of complex shockwave dynamics in laser ablation plumes in argon atmosphere, Phys. Plasmas **19**, 083504 (2012).

[40] P. K. Pandey, S. L. Gupta, and R. K. Thareja, Study of pulse width and magnetic field effect on laser ablated copper plasma in air, Phys. Plasmas **22**, 073301 (2015).

[41] E. Parkevich, G. Ivanenkov, M. Medvedev, A. Khirianova, A. Selyukov, A. Agafonov, A. Mingaleev, T. Shelkovenko, and S. Pikuz, Mechanisms responsible for the initiation of a fast breakdown in an atmospheric discharge, Plasma Sources Sci. Technol. **27**, 11LT01 (2018).

[42] J. R. de Bruyn, E. Bodenschatz, S. W. Morris, S. P. Trainoff, Y. Hu, D. S. Cannell, and G. Ahlers, Apparatus for the study of Rayleigh–Bénard convection in gases under pressure, Rev. Sci. Instrum. **67**, 2043 (1996).

[43] A. Gopal, S. Minardi, and M. Tatarakis, Quantitative two-dimensional shadowgraphic method for high-sensitivity density measurement of under-critical laser plasmas, Opt. Lett. **32**, 1238 (2007).

[44] K. Smaznova, A. Khirianova, E. Parkevich, M. Medvedev, E. Varaksina, T. Khirianov, A. Oginov, and A. Selyukov, Precise optical registration of fine-structured electrical sparks and related challenges, Opt. Express **29**, 35806 (2021).

[45] V. L. Ginzburg, *The Propagation of Electromagnetic Waves in Plasmas* (Pergamon, Oxford, 1970).

[46] M. A. Isakovich *et al.*, *General Acoustics* (Nauka, Moscow, 1973).

[47] V. I. Tatarski, *Wave Propagation in a Turbulent Medium* (Courier Dover Publications, Mineola, NY, 2016).

[48] S. M. Rytov, Y. A. Kravtsov, and V. I. Tatarskii, *Introduction to Statistical Radiophysics* (Springer, Berlin, 1978).

[49] B. Chen and J. J. Stamnes, Validity of diffraction tomography based on the first Born and the first Rytov approximations, Appl. Opt. **37**, 2996 (1998).

[50] S. Solimeno, *Guiding, Diffraction, and Confinement of Optical Radiation* (Elsevier, Amsterdam, 2012).

[51] J. W. Goodman, *Introduction to Fourier Optics* (Roberts and Company Publishers, Greenwood Village, CO, 2005).

[52] Y. A. Kravtsov and Y. I. Orlov, *Geometrical Optics of Inhomogeneous Media* (Springer-Verlag, Berlin, 1990), Vol. 38.

[53] E. V. Parkevich, A. I. Khiryanova, T. F. Khiryanov, D. V. Tolbukhin, Ya. K. Bolotov, and S. A. Ambrozevich, On the quantitative evaluation of laser diffraction by plasma formations with a micron-sized diameter, Bull. Lebedev Phys. Inst. **50**, 540 (2023).

[54] H. Hopkins, The frequency response of a defocused optical system, Proc. R. Soc. London A **231**, 91 (1955).

[55] E. Parkevich, M. Medvedev, A. Selyukov, A. Khirianova, A. Mingaleev, and A. Oginov, Laser-triggered gas switch with sub-nanosecond jitter and breakdown delay tunable over 0.1–10 ns governed by the spark gap ignition angle, Plasma Sources Sci. Technol. **29**, 05LT03 (2020).

[56] D. S. Volosov, *Photographic Optics* (Iskusstvo, Moscow, 1978) in Russian.

[57] E. Parkevich, M. Medvedev, A. Selyukov, A. Khirianova, A. Mingaleev, S. Mishin, S. Pikuz, and A. Oginov, Setup involving multi-frame laser probing for studying fast plasma formation with high temporal and spatial resolutions, Opt. Lasers Eng. **116**, 82 (2019).

[58] G. Sarkisov, Shearing interferometer with an air wedge for the electron density diagnostics in a dense plasma, Instrum. Exp. Tech. **39**, 727 (1996).

[59] S. Pikuz, V. Romanova, N. Baryshnikov, M. Hu, B. Kusse, D. Sinars, T. Shelkovenko, and D. Hammer, A simple air wedge shearing interferometer for studying exploding wires, Rev. Sci. Instrum. **72**, 1098 (2001).

[60] K. Bockasten, Transformation of observed radiances into radial distribution of the emission of a plasma, J. Optic. Soc. Amer. **51**, 943 (1961).

[61] P. Müller, Optical diffraction tomography for single cells, Dissertation, Biotechnology Center, Dresden University of Technology, Dresden (2016).

[62] Y. Cui, C. Zhuang, X. Zhou, R. Zeng, and J. He, Thermodynamic properties of negative discharge channels in a 1-m air gap measured by optical interferometry, IEEE Trans. Plasma Sci. **47**, 1917 (2018).

[63] Y. Cui, C. Zhuang, X. Zhou, and R. Zeng, The dynamic expansion of leader discharge channels under positive voltage impulse with different rise times in long air gap: Experimental

observation and simulation results, J. Appl. Phys. **125**, 113302 (2019).

[64] M. Du, Y. Tang, M. Li, J. Zou, Y. Ma, J. Sun, L. Liu, and Q. Zeng, Thermal characteristics of positive leaders under different electrode terminals in a long air gap, Energies **12**, 4024 (2019).

[65] D. Levko and L. L. Raja, High-voltage microdischarge as a source of extreme density plasma, Phys. Plasmas **25**, 013509 (2018).

[66] N. Minesi, S. A. Stepanyan, P. B. Mariotto, G.-D. Stancu, and C. O. Laux, On the arc transition mechanism in nanosecond air discharges, in *Proceedings of the AIAA Scitech Forum* (American Institute of Aeronautics and Astronautics, 2019), p. 0463.

[67] S. Shcherbanev, C. Ding, S. Starikovskaia, and N. Popov, Filamentary nanosecond surface dielectric barrier discharge. Plasma properties in the filaments, Plasma Sources Sci. Technol. **28**, 065013 (2019).

[68] N. Minesi, S. Stepanyan, P. Mariotto, G. D. Stancu, and C. Laux, Fully ionized nanosecond discharges in air: The thermal spark, Plasma Sources Sci. Technol. **29**, 085003 (2020).

[69] N. Q. Minesi, P. B. Mariotto, E. Pannier, A. Vincent-Randonnier, G. D. Stancu, and C. O. Laux, Kinetic mechanism and sub-ns measurements of the thermal spark in air, Plasma Sources Sci. Technol. **32**, 044005 (2023).

[70] B. Zhang, Y. Zhu, X. Zhang, N. Popov, T. Orrière, D. Z. Pai, and S. M. Starikovskaia, Streamer-to-filament transition in pulsed nanosecond atmospheric pressure discharge: 2D numerical modeling, Plasma Sources Sci. Technol. **32**, 115014 (2023).